Aeroacoustic investigation of side-by-side urban air mobility aircraft in full configuration with ground effect

Mohammad Sadegh Araghizadeh[1], Bidesh Sengupta[2], Hakjin Lee (이학진)[1*], Rho Shin Myong (명노신)[1]

[1]*School of Aerospace Engineering, Gyeongsang National University, Jinju, Gyeongnam 52828, South Korea*

[2]*Nanyang Technological University, Singapore 639798, Republic of Singapore*

[*]Author to whom correspondence should be addressed: hlee@gnu.ac.kr

Abstract

Urban air mobility (UAM) aircraft has emerged as the solution to the growing traffic congestion problems and increasing demand for efficient air mobility. However, noise pollution is one of the major concerns for gaining social acceptance as UAM is being designed for future transport in highly populated urban areas at low altitudes. The noise generated by UAM aircraft can exceed the acceptable noise level due to the ground effect when it approaches a vertiport. This study investigates the ground effects on the aerodynamic and noise performance of side-by-side UAM aircraft in full configuration by utilizing coupled vortex methods and acoustic analogy, respectively. The simulation results show that fuselage and ground directly influence the aerodynamic loads of the rotor blade, wake structure, acoustic signature, and noise directivity. As the aircraft approaches the ground, the sound pressure level (SPL) increases, and the impact of the fuselage becomes more noticeable, especially above the rotor system, due to the stronger upwash wake by the airframe and the ground. Moreover, the most pronounced ground effect on the noise characteristics of the UAM aircraft is the high-frequency tonal noise, and the overall sound pressure level (OASPL) in the aft quadrant of the UAM aircraft is higher than the forward quadrant due to the higher loading in the rear of the rotor plane. The results of the noise hemisphere analysis show that the maximum OASPL increases by more than 3 dBA as the altitude of UAM aircraft gets closer to the ground.

Keywords: Urban Air Mobility (UAM), Vortex Methods, Ground Effect, Aerodynamics, Aeroacoustics

1. Introduction

According to a United Nations report, more than 80% of the population in the developed regions are expected to live in urban areas by 2050. Rapid urbanization has considerably increased the energy consumption and environmental concerns. In recent decades, technological advancements in electric batteries and distributed propulsion have motivated the aviation industry to develop hybrid or fully electric vertical take-off and landing (eVTOL) aircraft with multiple lifting rotors or prop-rotors as novel air transport systems in highly crowded megacities as remedies for traffic congestion and transportation. Considering the significant market prospects in urban air mobility (UAM), numerous aviation companies and startups have developed prototypes and conceptual designs for UAM aircraft. Despite these investments and designs, several challenges and multidisciplinary constraints may slow the pace of successful applications. In addition to UAM safety standards, which have continuously been a primary concern owing to the UAM aircraft operations in urban areas, the noise emissions of these aircraft also raise concerns regarding compliance with the regulations for international and national noise exposure standards in residential areas. Since the UAM aircraft is expected to become a part of the public transportation system in highly populated cities, noise pollution is a considerable concern for health organizations [1–3]. Therefore, the noise generated by a UAM aircraft requires new noise standards that differ from those of a commercial rotorcraft [4–6].

Compared to conventional rotorcrafts, such as helicopters, the UAM aircraft exhibit two distinctive features [7, 8]. First, the aerodynamic interaction in a multirotor configuration is more complex than that in a conventional helicopter with a single main rotor. Distributed electric propulsion (DEP) systems utilize electrically driven propulsors that provide advanced capabilities for improving performance, design flexibility, high propulsion availability, and low community noise. However, the rotor interactional effects cause highly unsteady and complicated flow fields around neighboring rotors, which are directly related to the aerodynamic performance, development of wake geometry, vibration, and noise generation. Jia and Lee [9, 10] implemented a high-fidelity NASA (National Aeronautics and Space Administration) computational fluid dynamics (CFD) solver [11] and the acoustic prediction software PSU-WOPWOP [12]—a numerical implementation of Farassat's formulation 1A [13] of the Ffowcs Williams and Hawkings (FW-H) equation [14]—to investigate the acoustic characteristics of one- and six-passenger NASA conceptual quadrotor eVTOL aircraft and a lift-offset coaxial rotor in forward flight. The simulation results showed that the blade vortex interaction (BVI) is the most dominant source of interaction in the quadrotor eVTOL configuration. Diaz and Yoon [15] conducted an aeroacoustic analysis of a quadrotor

configuration under hovering and forward flight conditions by loosely coupling high-fidelity CFD with the comprehensive rotorcraft code of CAMRAD II. Their findings showed that the power required to maintain a steady cruise decreases in forward flight as the rotor–rotor interactions decrease. Rotor–rotor interactions are highly dependent on the positioning and orientation of the rotors with respect to each other. Dbouk and Drikakis [16] exploited open-source CFD code [17] to predict the noise generated by a swarm of multicopters. They found that the flight formation of aerial vehicles could also affect their acoustic behavior, with a V-shaped formation producing lower sound pressure level (SPL) noise than a U-shaped formation. Ko and Lee [18] examined the aerodynamic and aeroacoustic characteristics of multirotor configurations and their physical relationships with the performance and wake dynamics. Experimental setups have also been designed to investigate the acoustic [19] and psychoacoustic [20] characteristics of multi-rotor unmanned aerial vehicles (UAV). Ahuja et al. [21, 22] integrated Farassat's formulation 1A with a surface-vorticity solver to study two propeller configurations of a UAM aircraft—NASA X-57 propeller and Joby S4 UAM eVTOL propeller. Kim et al. [23] demonstrated that a UAM airframe shape and its distance from the rotor system can significantly affect the aeroacoustic characteristics of the aircraft using high-fidelity lattice-Boltzmann method with the FW–H equation with a permeable surface.

Fig. 1. Flight zone of commercial aircraft and a UAM vehicle

Second, as UAM aircraft are designed to operate primarily in residential areas, their operational safety is a high priority for aircraft designers. In addition, contrary to conventional helicopters, which have specific locations to land and take off, the vertiports for UAM vehicles are placed mainly on top of skyscrapers. The flight routes of commercial and UAM aircraft are compared in Fig. 1; as shown, the UAM vehicles frequently land and take off vertically at the vertiports [24, 25]. During the vertical maneuvers near the vertiport, the strong interactions between the UAM aircraft and the vertiport, known as ground effects, can directly affect the flight dynamics, aerodynamic performance, wake development [26, 27], and noise generation [28]. Investigating the impact of

ground effects on a UAM aircraft is imperative to ensure safe operation and to avoid accidents that may occur during vertical take-off and landing near the ground. Several studies have previously investigated the influence of ground effects on the performance of helicopters through computational and experimental approaches [29–32]. Ramasamy et al. [27, 33] conducted an experimental investigation on a scaled CH-47D tandem rotor. Tan et al. [34] studied the effects of crosswinds on the flow field of an EH-60L helicopter brownout flight by coupling a vortex-based solver with the discrete element method.

The objective of this work is to numerically study the interactional aerodynamic and acoustic characteristics of a completed configuration of a six-passenger side-by-side (SbS) UAM aircraft near the ground using reliable and fast mid-fidelity vortex methods. The influence of ground effects on the rotor performance, wake structure, and noise level were investigated at different heights from the ground. Table 1 summarizes the recent studies on the NASA SbS eVTOL aircraft [35]. From the literature, two major gaps in the reported works on the aerodynamic and acoustic analysis of UAM aircraft can be identified. First, there is limited research focusing on the computational simulation of UAM aircraft in full configurations, even though Sagaga and Lee [36, 37] conducted the high-fidelity computational study of the side-by-side rotor in full configuration. Although the high-fidelity CFD method can describe the detailed flow physics, it requires the high computational costs and a complicated numerical setup as the number of rotors or propellers increases. On the contrary, the method proposed in this study is able to predict fairly good results across a reasonably wide spectrum of flow conditions. Second, to the best of our knowledge, no numerical investigation has been conducted on the influence of ground effects on the full configuration of a UAM aircraft. The flow regime of a multirotor system near the ground is highly unsteady and depends on the airframe of the rotorcraft and rotor system configuration, which makes studying UAM performance a unique challenge as one aircraft design could have an entirely different behavior from another.

Table 1. Detailed review of aerodynamic and acoustic analysis of the SbS UAM aircraft

Paper details	Model	Ground effect	Numerical methods
Diaz et al. [38] (2019)	Isolated rotor	out-of-ground effect (OGE)	- High-fidelity CFD solver - High computational cost
Jia and Lee [39] (2022)	Isolated rotor	out-of-ground effect (OGE)	- High-fidelity CFD solver - Acousic analogy - High computational cost

Sagaga and Lee [40] (2023)	Isolated rotor	In-ground effect (IGE)	- High-fidelity CFD solver - Acousic analogy - High computational cost
Present (2024)	Full configuration	In-ground effect (IGE)	- Coupled vortex method with VPM - Acoustic analogy - Comparatively very low cost

In this study, we used a nonlinear vortex lattice method (NVLM) coupled with source-doublet panel methods to simulate the flow over the rotor blade, fuselage, and ground. The rotor wake field was modeled using the time-accurate vortex particle method (VPM), which efficiently describes the unsteady wake flow. Moreover, Farassat's formulation 1A was utilized to assess the tonal noise in terms of the thickness and loading noise associated with the blade passing frequency [41] as the dominant noise source of the SbS UAM aircraft is the loading noise [42]. The rest of the paper is organized as follows. Section 2 overviews the numerical model for the aerodynamic and aeroacoustic parts. Section 3 provides some of the validations for the model and introduces the computational setup and NASA side-by-side air taxi. A discussion and comparison of the obtained results are given in section 4. Finally, concluding remarks are made in Section 5.

2. Numerical Methods

2.1 Coupled vortex method

Despite significant advances in computational capabilities in recent years, conducting aerodynamic and acoustic analyses of the SbS eVTOL aircraft in a full configuration and considering ground effects using high-fidelity CFD methods remains computationally demanding. In this study, we used a coupled vortex method composed of the NVLM, source-doublet panel method, and VPM to effectively assess the influence of ground effects on the aerodynamic and noise performance of the SbS eVTOL aircraft. Assuming that the rotor blades were sufficiently thin, the NVLM was implemented to simulate the SbS rotor. The fuselage and ground were represented by source-doublet panels with constant strength, and the wake structures generated by the two rotors were modeled by vortex particles. The explanations of each numerical method are as follows.

Vortex methods assume that the flow is inviscid, incompressible, or irrotational. Therefore, the continuity equation in terms of the velocity potential ϕ can be written as a Laplace equation. The general solution to the Laplace equation can be derived using Green's second identity. It is represented by a sum of elementary or singular solutions, such as source σ and doublet μ distribution on the body surfaces S_B or only doublet distribution on the

wake surface S_w as the wake surface is assumed to be thin. The VLM also called the lifting surface method, is based on the assumptions of the thin lifting surface theory. If the rotor blade is considered thin, it can be regarded as a lifting surface without thickness, which nullifies the source term in the Laplace equation, and only the doublet distribution remains. The rotor blade and wake are modeled using the vortex ring elements because the constant-strength doublet element is equivalent to a constant-strength vortex ring element with the same strength ($\Gamma = \mu$). Although the VLM is an efficient and reasonably accurate method of modeling the rotor blade, it cannot consider nonlinear aerodynamic characteristics mainly associated with viscosity, flow separation, and low-Reynolds-number flow. Therefore, a novel NVLM, which incorporates a VLM with airfoil lookup tables, semi-empirical aerodynamic models, and vortex strength correction, is introduced to overcome these limitations. The NVLM was also tightly coupled with the VPM to simulate unsteady wake dynamics. Details of the numerical strategies used in the NVLM and VPM are provided in [43].

Contrary to the rotor blade thickness, those of the fuselage and ground cannot be neglected. The thickness effect can be applied based on the distribution of the source terms on the surface. In the source-doublet panel method, to find a unique solution for the Laplace equation, along with the no-penetration boundary condition and Kutta condition, a Dirichlet boundary condition must also be applied to the problem in which the source term is calculated using the normal product of the free-stream velocity [44]. The panel method is weakly coupled with the NVLM, as depicted in Fig. 2, which enables the creation of the influence matrix of the non-deformed geometry (fuselage and ground) before the beginning of the main loop, effectively reducing the computational cost of this model. After solving a linear system of equations for the blade, the strengths of the vortex lattices on the blade are updated using empirical lookup tables. Thereafter, the vortex particles of the wake are convected using a time-marching scheme. The aerodynamic data for noise calculation are exported at the end of each iteration. The iterations are stopped when the aerodynamic load of the rotorcraft converges to a stable condition. Fig. 3 illustrates the coupled vortex method for simulating side-by-side rotorcraft: vortex lattices consisting of four vortex filaments are used for representing the rotor blades, and Kutta wake panels, and the source-doublet panels with constant strength are utilized for modeling the fuselage and ground.

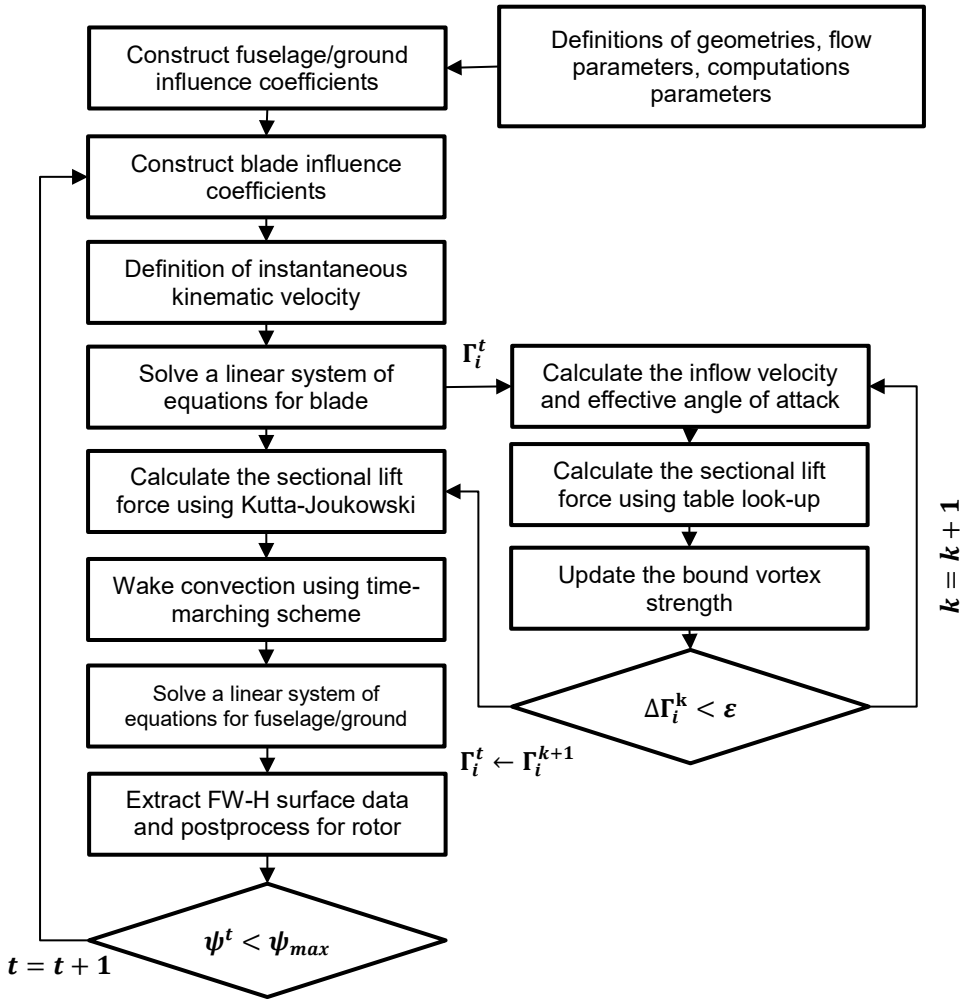

Fig. 2. Flowchart of coupled vortex method for simulating side-by-side UAM aircraft in full configuration

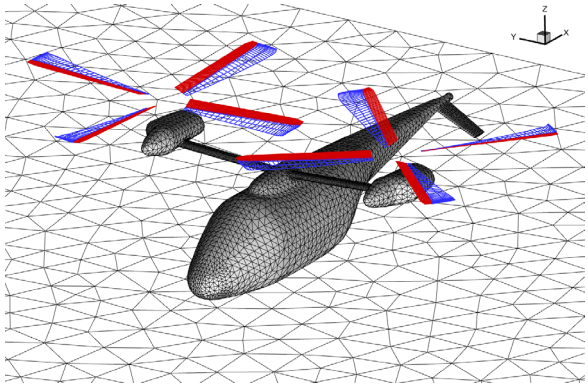

Fig. 3. Vortex lattices and source-doublet panels used to simulate the SbS rotorcraft in ground effect

2.2 Vortex particle method

The rotor wake originating from the blade must be described using the Lagrangian approach rather than the Eulerian approach. The Lagrangian VPM can accurately simulate the complex wake field of a rotorcraft without the numerical dissipation error caused by the volume discretization with the grid. This study tightly integrated the NVLM with a time-accurate VPM to simulate the wake flow around the SbS rotor configuration. Unlike in the vortex filament method, the vortex particles do not necessarily need to maintain connectivity with the adjacent particles, allowing them to freely be deformed and transported downstream. These features make the VPM helpful in capturing the dynamic and unsteady behavior of the wake field originating from the rotor-to-wake or wake-to-wake interactional effects.

During the time-marching step for developing the wake, the rotor blade rotates, and blade vortex elements placed on the trailing edge are shed with a local convection velocity and move downstream. In the initial time steps, the trailed and shed wake vortex filaments that originated from the blade are modeled as curved vortex filaments. Subsequently, they are discretized into a finite number of vortex particles. Each vortex particle is later convected away from the rotor by the sum of the freestream velocity and the velocity induced by the bound vortices of the rotor blades, fuselage/ground panels, and other vortex particles. The Biot–Savart law is implemented to calculate the velocity of one particle induced by the other vortex particles in the wake field, which is represented by a set of p Lagrangian vector-valued vorticity particles. The velocity induced at the mth vortex particle by vortex particles (n = 1, 2,…, p) can be expressed using Eq. (1), where m and n are vortex particle indices, $\boldsymbol{x}_m$ is the position vector of the Lagrangian vortex particles, and p is the total number of vortex particles. $\boldsymbol{\alpha}_n$ is the vector-valued total vorticity inside nth particle; σ_{mn} is a symmetrized smoothing parameter for preventing the singularity problem, and ρ is the non-dimensional distance parameter. The relationships between these parameters can be expressed as follows:

$$\mathbf{V}_{ind.particles}(\mathbf{x}_m, t) = -\sum_{n=1}^{p} \frac{1}{\sigma_{mn}^3} K(\rho)(\mathbf{x}_m - \mathbf{x}_n) \times \boldsymbol{\alpha}_n \tag{1}$$

$$\sigma_{mn} = \frac{\sqrt{\sigma_m^2 + \sigma_n^2}}{2} \tag{2}$$

$$\rho = \frac{|\mathbf{x}_m - \mathbf{x}_n|}{\sigma_{mn}}, \tag{3}$$

where σ is the core radius of the particles, σ_m is the core radius for the particle m at which the induced velocity from the particle n is calculated. $K(\rho)$ is the regularized kernel for evaluating the induced velocity, which is formulated using the vorticity distribution function and the Green function for the vector stream function. Various forms of the distribution function are available; however, the three-dimensional high-order algebraic smoothing function proposed by Winckelmans and Leonard [45] is used here:

$$K(\rho) = \frac{G(\rho) - \xi(\rho)}{\rho} \tag{4}$$

$$G(\rho) = \frac{1}{4\pi} \frac{\rho^2 + 3/2}{(\rho^2 + 1)^{3/2}} \tag{5}$$

$$\xi(\rho) = -\frac{1}{\rho} \frac{d^2}{d\rho^2} [\rho G(\rho)] = \frac{15}{8\pi} \frac{1}{(\rho^2 + 1)^{7/2}} . \tag{6}$$

To achieve wake evolution, the convection velocities of the vortex particles are evaluated at each time step, and their locations are determined using the second-order Runge–Kutta method. The rotation speed of the rotor blade is gradually increased from zero to the designated speed, and its variation is defined using a sine function. For further details, please refer to our previous report [43].

2.3 Noise prediction method

The noise signal propagating from a rotor is typically categorized into non-deterministic and deterministic components. The former signals arise from turbulence ingestion noise, blade–wake interaction noise, and airfoil self-noise, whereas the latter arise from thickness noise, loading noise, BVI noise, and high-speed impulsive noise. The thickness and loading noise of the deterministic components are primarily linked to the rotating blades, resulting in periodic and tonal noise characteristics that lead to a high SPL at the rotor blade passage frequency (BPF) and its harmonics. Thickness noise occurs because of the flow disturbance caused by the moving rotor blades, and loading noise is generated by the time-varying aerodynamic loads acting on the blade surface.

The current study primarily focused on predicting the thickness and loading noise generated by the SbS rotor configuration rather than non-deterministic configurations. The SPLs of the thickness and loading noise were evaluated through the numerical implementation of Farassat's formulation 1A, which is a solution to the FW-H equation that neglects the quadrupole source term [13, 46]. Farassat's formulation 1A is an integral method for evaluating aerodynamically generated noise. The thickness and loading noise were modeled using surface sources

in terms of monopole and dipole sources. The acoustic pressures of the thickness ($P'_T(\mathbf{x}, t)$) and loading ($P'_L(\mathbf{x}, t)$) noise sources can be calculated as follows:

$$p'(\mathbf{x},t) = p'_T(\mathbf{x},t) + p'_L(\mathbf{x},t) \tag{7}$$

$$p'_T(\mathbf{x},t) = \frac{1}{4\pi}\int_{f=0}\left[\frac{\rho_0(\dot{v}_n + v_{\dot{n}})}{r\left|1-M_r\right|^2}\right]_{ret} dS + \frac{1}{4\pi}\int_{f=0}\left[\frac{\rho_0 v_n (r\dot{M}_r + a_0 M_r - a_0 M^2)}{r^2\left|1-M_r\right|^3}\right]_{ret} dS \tag{8}$$

$$\begin{aligned} p'_L(\mathbf{x},t) = {} & \frac{1}{4\pi a_0}\int_{f=0}\left[\frac{\dot{l}_r}{r\left|1-M_r\right|^2}\right]_{ret} dS + \frac{1}{4\pi}\int_{f=0}\left[\frac{l_r - l_M}{r^2\left|1-M_r\right|^2}\right]_{ret} dS \\ & + \frac{1}{4\pi a_0}\int_{f=0}\left[\frac{l_r\left(r\dot{M}_r + a_0 M_r - a_0 M^2\right)}{r^2\left|1-M_r\right|^3}\right]_{ret} dS \end{aligned} \tag{9}$$

where $[\ \ ]_{ret}$ signifies the evaluation of the enclosed quantity at the retarded time (τ):

$$\tau = t - \frac{r}{a_0} = t - \frac{|\mathbf{x}-\mathbf{y}|}{a_0} \tag{10}$$

τ is the retarded time when the sound is emitted from sources, whereas t is the observer time. Further, a_0 is the speed of sound, ρ_0 is the density of air, and r is the distance between the source ($\mathbf{x}$) and observer ($\mathbf{y}$) positions [41]. Subscripts n and r denote the quantities in the normal direction to the blade surface and radiation direction, respectively, that is, v_n is the local normal velocity of the blade surface. l indicates the local loading that acts on the fluid due to the blade surface and M_r is the Mach number in the radiation direction.

3. Numerical Setup

3.1 Validation

The NVLM has been previously applied to various rotor blades to predict their aerodynamic performance, and its predictive capability has been validated in several studies [41, 43, 47–49]. Two well-known experimental studies were conducted to validate the panel and coupled vortex methods. First, the panel code model simulated the flow around the isolated ROBIN fuselage at an angle of attack of 0°. The predictions of the surface pressure coefficients at different longitudinal stations were compared with the experimental data [50] and simulation results obtained using FUN3D—an unstructured mesh-based Reynolds-averaged Navier–Stokes (RANS) method [51]—as illustrated in Fig. 4. The pressure predictions are well-matched with the experimental and numerical results at most points, particularly the points at which there is no flow separation from x/l = 0.0517 to x/l = 0.3497 (here, l

is the half of the fuselage length). At x/l = 0.4669, the FUN3D results predict a small separation at z/R = 0.12 near the nacelle at the top of the fuselage, but the panel method fails to predict the separation, and the flow continues to accelerate because it is a potential code. Neglecting the fuselage strut and rotor shaft in the numerical models causes discrepancies between their results and the experimental data at points along the bottom and top of the fuselage, respectively (see Fig. 4 (d)).

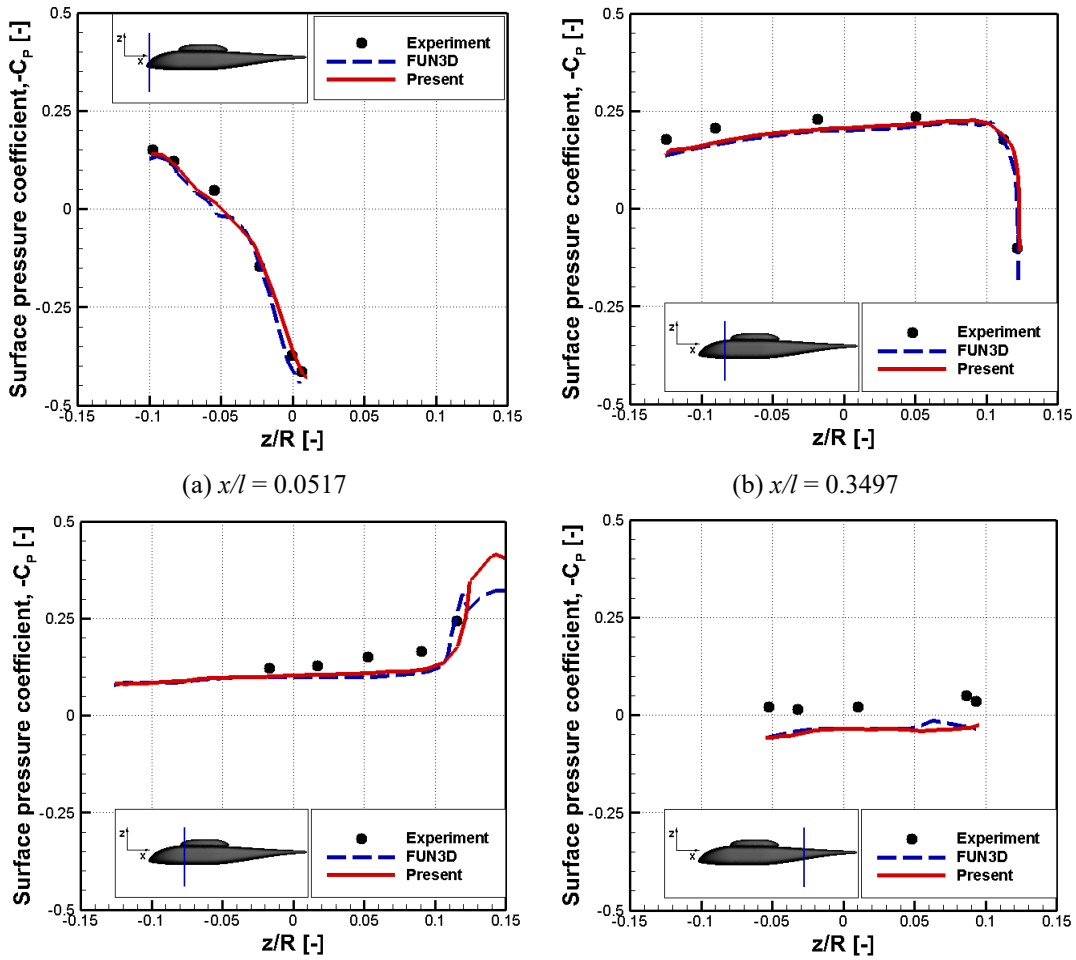

(a) x/l = 0.0517 (b) x/l = 0.3497

(c) x/l = 0.4669 (d) x/l = 1.3450

Fig. 4. Comparison of the steady pressure distribution on isolated fuselage at M_∞ = 0.062

The numerical results for the in-ground effect (IGE) and out-of-ground effect (OGE) of an isolated rotor were validated by Light's experiment on a four-bladed full-scale Lynx tail rotor hovering with a tip Mach number of 0.56 [52]. The rotor had constant chords and untwisted blades. The radius and blade aspect ratio were 1.105 m and 6.14, respectively. The blade section was composed of NPL9615 airfoil. Fig. 5 compares the axial and radial locations of the tip vortices according to the experimental data and the numerical results obtained using the

vorticity transport model (VTM) [53] and RANS [54]. VTM is a finite volume-based method exploiting the vorticity-velocity form of the incompressible Navier-Stokes equation. In this method, the vorticities evolve in the flow by velocity, which is calculated by the Biot-Savart law. The RANS results were obtained using FLOWer code, which is an open-source CFD code. As Fig. 5 shows, the RANS method over-predicts the radial contraction of the tip vortices in some cases and predicts a higher axial descent rate after the first blade passage. The coupled vortex methods used in this study produced results that agreed well with the experimental data and were comparable to other numerical models. The predicted thrust coefficient and figure of merit were compared with the experimental data at different rotor heights and constant collective pitch angles, as listed in Table 2. The values were normalized to the OGE values. Again, the computational and experimental results agree well. Moreover, as expected, the rotor thrust and performance increased with decreasing rotor height above the ground during hovering, as observed during the experiments.

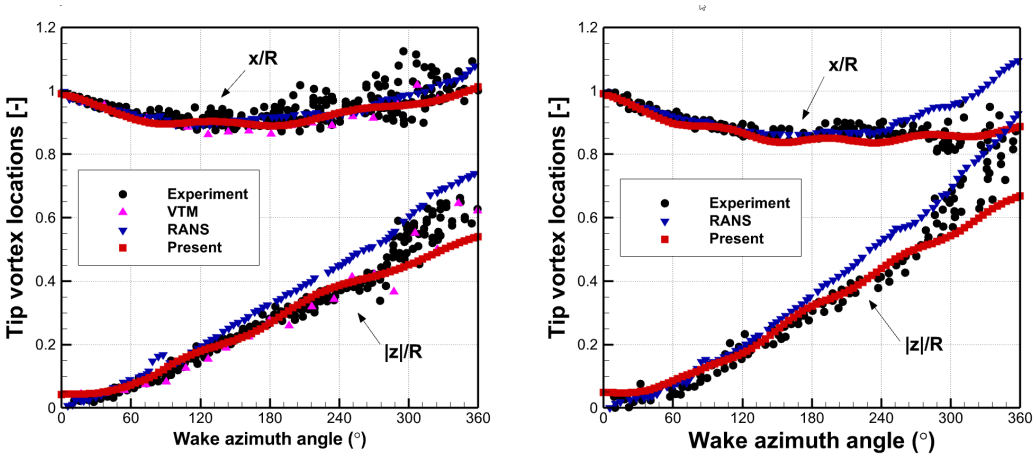

(a) IGE, H/R = 0.84, C_T/σ = 0.071

(b) IGE, H/R = 1.54, C_T/σ = 0.08

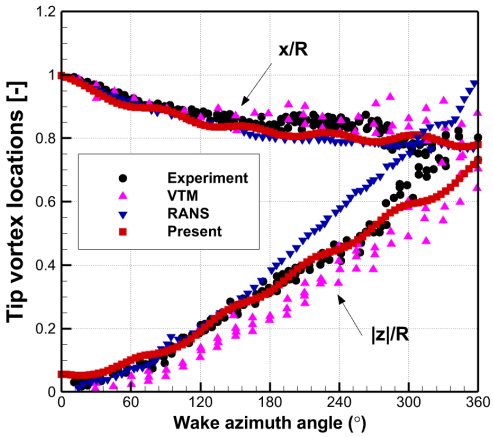

(c) OGE, C_T/σ = 0.09

Fig. 5. Tip vortex axial and radial locations of the Lynx tail rotor

Table 2. Comparison of thrust and FM between predictions and measurements [52] at different rotor heights

	$C_T/C_{T,OGE}$			FM/FM_{OGE}		
h/R	Experiment	Present	Error (%)	Experiment	Present	Error (%)
4	1	1	0	1	1	0
1.92	1.022	1.024	0.2	1.018	1.027	0.88
1.54	1.032	1.058	2.52	1.047	1.059	1.15
0.95	1.090	1.110	1.83	1.150	1.110	3.48

The acoustic analogy of our model was previously validated for an isolated rotor configuration [41]. The acoustic amplitude and directivity behavior of the rotor blade well matched between the experimental data and numerical results of the coupled analysis using high-fidelity CFD and acoustic solvers. Moreover, the aeroacoustics results for the full configuration of side-by-side rotorcraft of the present model are compared with the high-fidelity computational study of the same configuration by Sagaga and Lee [36, 37]. They used CREATETM-AV Helios [55], with OVERFLOW as the near-body solver and SAMCart as the off-body solver, and for the acoustic predictions, they exploited PSU-WOPWOP, and their grid size is between 300-700 million depending on using adaptive mesh refinement. The UAM is in hovering mode with 499.97 RPM. The blade collective pitch angle for the study is 8 degrees. Although the OASPL-A calculated by the present model is 76.2 dBA which is lower than that of high-fidelity model which is 80.7 dBA, it was confirmed that reasonable noise level could be evaluated compared to the high-fidelity analysis results. Unlike reference [36, 37], the hub configuration is not simulated here. Moreover, the details of blade geometry could be different slightly. Although the numerical model used in this study is an efficient way to simulate the full configuration of the UAM vehicle, it cannot accurately capture the non-deterministic acoustic components.

In this study, only time-series data after 10 revolutions were utilized to acquire the acoustic results in the frequency domain rather than the overall time history across all revolutions. This post-processing technique can help accurately capture tonal acoustic amplitudes at the principal frequencies of interest. The time-series data were processed using a fast Fourier transform with a Hanning window function to isolate the acoustic contributions of different frequencies. The acoustic spectrum was converted into an SPL in decibels, and the resultant A-weighted overall SPL (OASPL) was computed by integrating the SPL spectrum.

3.2 Side-by-Side eVTOL aircraft

The aircraft prototype investigated in this study was a publicly available NASA OpenVSP model of the SbS UAM vehicle [56]. The landing gear and strakes were omitted in this study. The grid system consisted of a main fuselage, wing, engine, tail, and rotor. The SbS eVTOL aircraft is a representative high-performance rotorcraft comprising two rotors that interact aerodynamically with each other because they physically overlap and intermesh. The interaction of the main rotors is intended to reduce the induced power during forward flight. Further details of this aircraft can be found elsewhere [37, 39, 40]. For all instances of the SbS aircraft in this demonstration, the relative rotor phasing was held constant, and the phase shift between rotors was 45°. The separation distance (d), which is a typical characteristic in multirotor systems, is defined here as the distance between the hubs of two rotors, which for this configuration corresponds to 85% of the radius of the rotor (d/R = 0.85). Thus, overlapping rotors are more efficient in cruising than two isolated rotors, and the best setup is that with 15% rotor overlap which is overlapped distance scaled by the rotor radius. The hub-to-hub separation distance is 1.7R [37, 57-59]. The rotors were articulated with four blades per rotor and were controlled via collective and cyclic pitch angles. Because the material properties of the conceptual designs were not available, the rotor blades were assumed to be rigid. The rotor blades of the SbS rotor were modeled based on two modern airfoils: Boeing VR-12 and Sikorsky SSC-A09. VR-12 was used for r/R < 85% span, a linear interpolation between VR-12 and SSC-A09 was assumed to range from 85% to 95%, and SSC-A09 was used for r/R > 95% span. The chord length of the blade was 0.217 m until r/R = 94%, at which point the blade tapered. The slope of the linear twist distribution was assumed to be –16°, and the 0° twist occurs at a 75% span. A 15° linear taper ratio was applied between r/R = 94% and the blade tip. The fundamental specifications of these vehicles are listed in Table 3.

Table 3. Specifications of NASA SbS eVTOL aircraft

Parameter	Value
Overlap ratio [%]	15
Number of rotors [-]	2
Number of blades [-]	4
Rotor radius, R [m]	3.203
Root cutoff, R_{cut} [%]	16
Rotor solidity, σ [-]	0.0832
Gross weight, W [kg]	1792
Tip Mach number, M_{tip} [-]	0.484

3.3 Aeroacoustic simulation setup

The surface grids for the numerical simulation of the SbS aircraft are depicted in Fig. 6, where each blade is discretized with 720 quadrilateral vortex lattices, and the fuselage is represented by 9,188 unstructured triangular source-doublet panels. The grid system comprised the main fuselage, wing, engine, tail, and rotors, and the landing gear and strakes were omitted in this study. The rotor on the starboard side rotates counterclockwise (CCW), and the rotor on the port side rotates clockwise (CW). This study presents the instantaneous velocity magnitude contour at the mid-plane (Z-X plane in the middle of the aircraft) section, which will be discussed in detail later. The time-step size was set at a 3.0° azimuth for each time step for 12 rotor revolutions. The rotor azimuth angle (ψ_R) was defined in relation to the CCW rotation of the rotor on the starboard side (see Fig. 6). The rotational speed and pilot inputs for all the cases were constant. The rotor aerodynamic coning angle (β_0), collective pitch (θ_0), lateral cyclic pitch (θ_{1c}), and longitudinal cyclic pitch (θ_{1s}) of both rotors are listed in Table 4. The total thrust produced by the rotor system is greater than the gross weight of the eVTOL aircraft. In this study, the eVTOL aircraft was placed at different heights (h), which is the distance between the rotor hub and the ground, to investigate the ground effects on the aerodynamic performance and noise level of the aircraft in hovering flight conditions of h/R = 1 and h/R = 2.

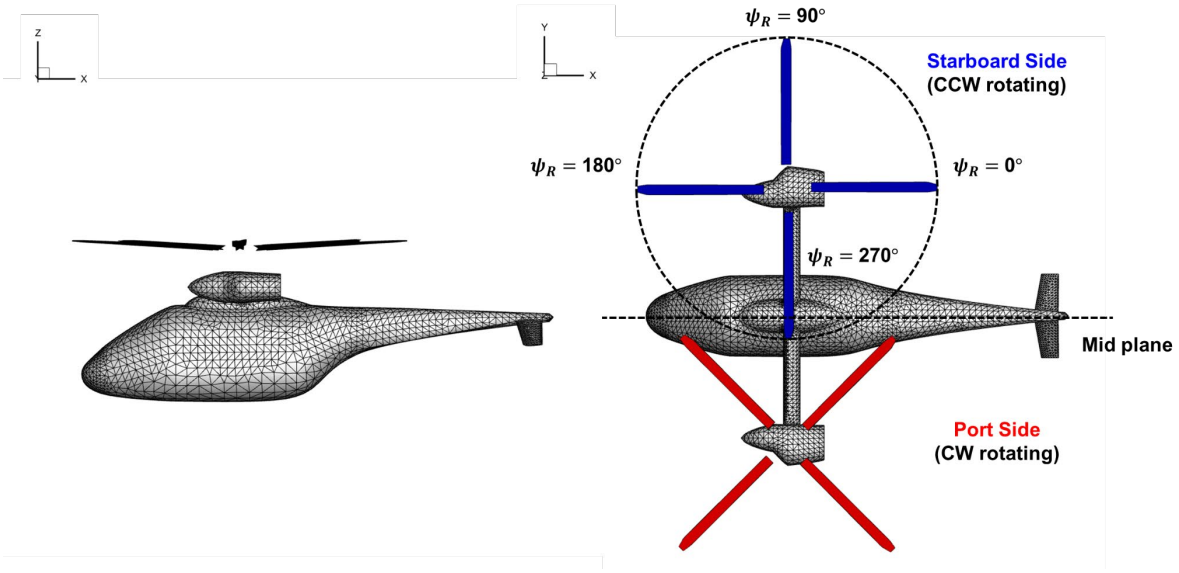

Fig. 6. Surface grid of the SbS eVTOL aircraft with 15% overlap and four tapered blades and definitions of mid-plane and rotor azimuth angle.

Table 4. Basic properties of the SbS UAM vehicle

Parameter	Value
Coning angle (β_0) [°]	3.1
Collective pitch (θ_0) [°]	12.2
Lateral cyclic pitch (θ_s) [°]	0.0
Longitudinal cyclic pitch (θ_c) [°]	0.0
h/R	1, 2

In this study, two distinct sets of microphone arrays were used to assess the noise performance of an eVTOL aircraft. Both arrays, with a circular arrangement of 36 microphones and a radial distance of 50 m ($\approx 8R$), were centered around the eVTOL aircraft, maintaining a 10° spacing between adjacent microphones. The placement of microphones in a circular arrangement provides a better estimation of noise directivity around the aircraft. The azimuth angle of the microphones (ψ_{MIC}) was defined as the same as the rotor azimuth angle, following a CCW direction. It is crucial to note that the positions of these arrays were adjusted for the OGE and IGE conditions. For the OGE condition, the microphone array was positioned 150 m ($\approx 24R$) below the eVTOL aircraft, facilitating the examination of fuselage effects, as depicted in Fig. 7(a). However, for the IGE condition, the microphone array was situated in the rotor disk plane to explore the variations in noise characteristics with varying ground proximity (see Fig. 7(b)). The acoustic characteristics were recorded for each observer and post-processed to retrieve the characteristic metrics at each observer location.

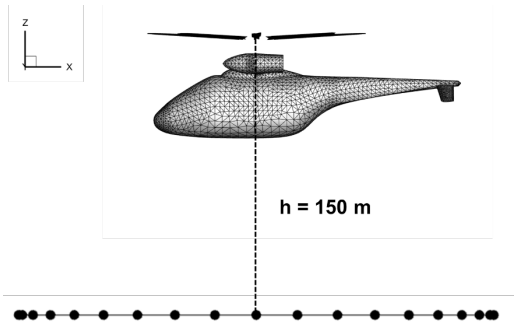

(a) Side view of the microphone locations (not drawn to scale)

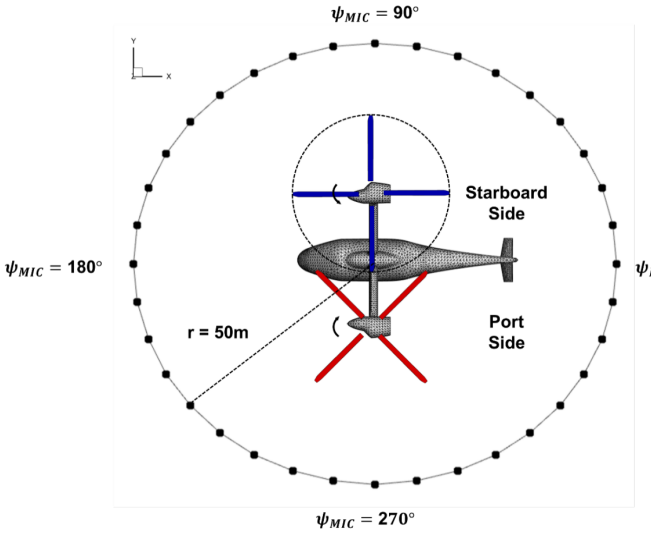

(b) Top view of the microphone locations (not drawn to scale)

Fig. 7. Acoustics simulation setup: microphone locations

4. Results and Discussion

The first part of this section discusses the influence of fuselage on the aerodynamic and acoustic characteristics of the SbS eVTOL under OGE conditions. The next section discusses the influence of the ground effect on the performance of the SbS aircraft in hovering mode. Hovering above the ground is a critical phase during the take-off and landing of UAM aircraft. Hence, the ground effect must be explored in hovering flight conditions to ensure the safety and reliability of eVTOL aircraft during landing and take-off operations. A consistent contour legend was used in all cases to facilitate a more effective comparison of the findings. The features of the case studies are listed in Table 5.

Table 5. Case studies for investigating the effects of the fuselage and ground

Case	Rotor model	Fuselage	Ground
1	SbS rotors with 15% overlap	No	No
2		Yes	No
3		Yes	Yes
4		Yes	Yes

4.1 Fuselage effect

The fuselage of a rotorcraft plays essential roles in its aerodynamic and aeroacoustic performance. This section addresses the effects of the fuselage on the aerodynamics, flow field, wake structure, and acoustics of the SbS

aircraft during hovering under OGE conditions. Accordingly, we selected Cases 1 and 2 from Table 5. The instantaneous velocity magnitude contour at the mid-plane (as defined in Fig. 6) and wake field for both the isolated rotor and full configuration in the OGE are depicted in Figs. 8 and 9, respectively. The wake structure is visualized with the color transition between blue and red, which red indicates the highest vorticity magnitude of the vortex particles while blue indicates the lowest vorticity magnitude of the vortex particles. The observed asymmetry in the longitudinal direction of the rotorcraft can be attributed to the rotational movement of the two rotors, which is CCW for the starboard rotor and CW for the port rotor. The counter-rotating directions of the SbS rotor system channel the downward flow. This phenomenon can also be observed in other multirotor cases, such as in the experimental investigation of tandem rotors [27]. Fig. 8 shows the presence of a counter-rotating-tip vortex pair emanating from a downstream rotor blade. For the isolated rotor case (see Fig. 8(b)), the structure of the counter-rotating tip vortex pair is asymmetrical, contributing to the longitudinal instability of the rotorcraft. However, the fuselage under the rotor system affects the evolution of the tip vortices, thus mitigating the asymmetric structure. The fuselage of the SbS aircraft favorably affects the stability of the rotorcraft downwash, leading to a decrease in its magnitude. The velocity contour also shows the occurrence of an upwash flow in the region between the rotor blade and fuselage, causing an increase in the thrust generated by the rotor system with the fuselage. This feature is further demonstrated by the vortices reflected above the fuselage in the wake structure of the SbS rotorcraft. The effect of the fuselage on the induced inflow ratio at $z/R = 0.12$ in the mid-plane (between the rotor system and the fuselage) is plotted in Fig. 10. The inflow ratio is defined as follow:

$$\lambda_i = \frac{w_i}{\Omega R} \tag{11}$$

Here w_i is the induced velocity, and Ω is the rotor angular velocity. Fig. 10 shows that the fuselage induced an upwash flow under the rotor system, which consequently reduced the downwash and increased the thrust of the rotor system. The upwash flow at the aft side of the fuselage is stronger than that of the fore side. A more intense wake interaction for the full configuration in the space between the fuselage and rotor system is evident in Fig. 9. Moreover, the vortices reflected from the fuselage contributed to the increased flow unsteadiness, particularly in the downward direction of the airframe.

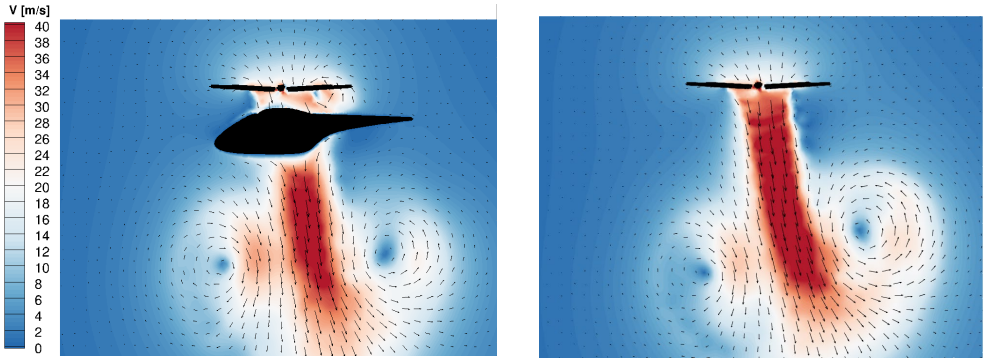

(a) SbS rotors with fuselage (b) SbS rotors without fuselage

Fig. 8. Comparison of the instantaneous velocity magnitude at mid-plane (side view: x-z plane)

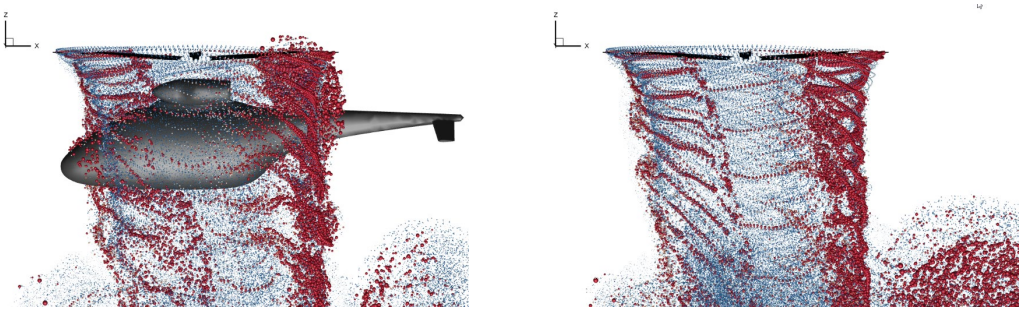

(a) SbS rotors with fuselage (b) SbS rotors without fuselage

Fig. 9. Comparison of wake structures at mid-plane (side view: x-z plane)

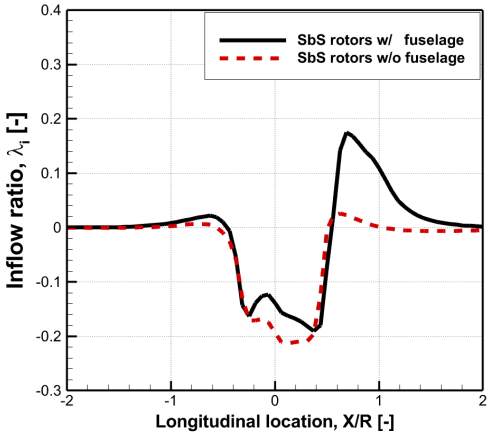

Fig. 10. Comparison of induced inflow ratio for isolated rotor and full configuration aircraft at $z/R = 0.12$ along the longitudinal direction

The collision of the strong tip vortices shed from one blade with the preceding blade results in a sudden change in the effective angle of attack of the rotor blade, eventually leading to impulsive loading. More sudden changes may occur if the interaction between the vortex and blade occurs in a shorter period (i.e., with higher frequency). Although the most pronounced changes occur because of the tip vortices, the collision of the shedding and trailing

vortices that depart from the blade trailing edge with other blades, known as blade–wake interactions, influence their aerodynamic performance. Fig. 11 compares the variations in the integrated thrust coefficient of the SbS rotor blades for the isolated and full configuration cases in one revolution. Both cases demonstrate impulsive aerodynamic loads induced by the BVI, resulting in impulsive pressure differentiation and noise. The presence of the fuselage amplifies the load peaks and increases the loading vibration amplitude, as shown in Fig. 11. The vibratory load of the rotor system resulting from an unsteady aerodynamic environment generates acoustic noise and vibration, enhancing the structural vulnerability and acoustic annoyance of the aircraft.

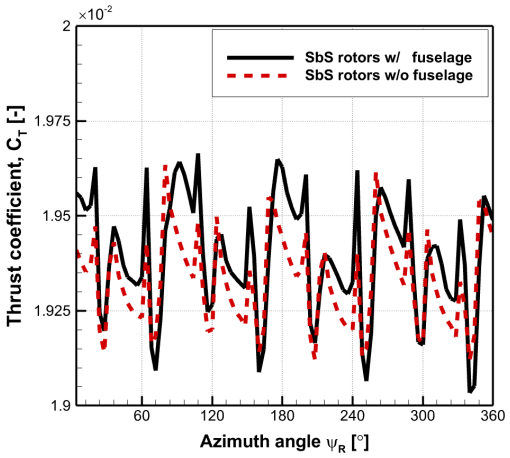

Fig. 11. Time variation in thrust coefficient for one revolution of isolated rotor and full configuration

The predictions of the acoustic pressure at microphone azimuth angles (ψ_{MIC}) of 0° (aft side), 90° (starboard side), 180° (fore side), and 270° (port side) are presented in Fig. 12. As mentioned earlier, the microphones are placed 150 m (≈47R) below the aircraft in a circular arrangement with a radial distance of 50 m (≈15R). Both the full configuration and isolated rotor cases exhibit high-frequency noise in all directions owing to the nature of the SbS rotor system and the resulting complex aerodynamic interactions [60], as shown in Fig. 9. The acoustic pressures for the observers at azimuth angles of 90° and 270° are quite similar, with a slight dissimilarity possibly attributed to the phase shift and highly complex vortex flow in the inter-rotor region for the overlapped rotors [60]. Furthermore, the existence of a fuselage increases the amplitude of the acoustic waves propagating toward these observers. However, for the microphones at ψ_{MIC} = 0° and 180°, the SPL differs as expected due to the asymmetry flow in the longitudinal direction. The peak-to-peak amplitudes of the impulses for the aft side observer of the rotorcraft is more than that of fore side observer. The effects of the fuselage on the overall sound pressure recorded by these microphones are also dissimilar. For the aft-side observer, the figure indicates that the rotor system with

the fuselage generates a greater impulse amplitude at the SPL than the isolated rotor, as shown in Fig. 12 (a). This finding implies that the airframe of the SbS UAM vehicle has a greater impact on the noise characteristics in the forward direction of the aircraft.

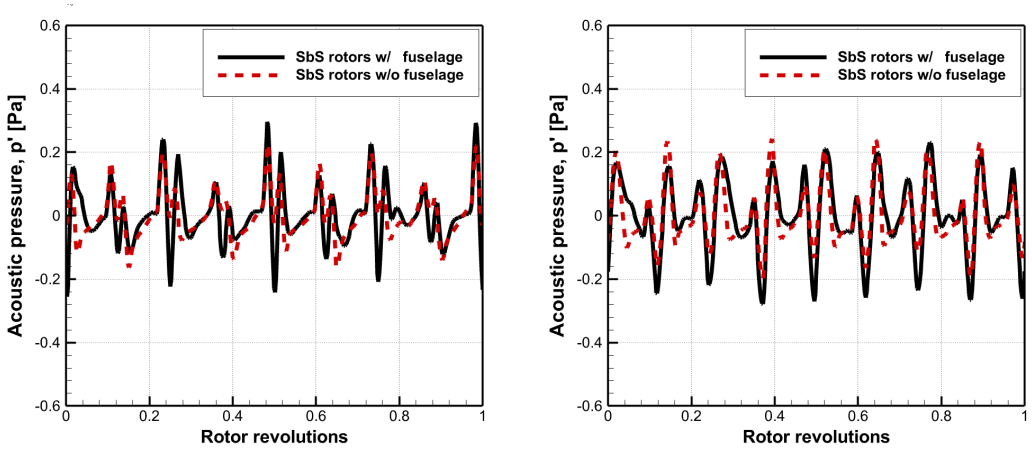

(a) Observer at Ψ_{MIC} = 0°

(b) Observer at Ψ_{MIC} = 90°

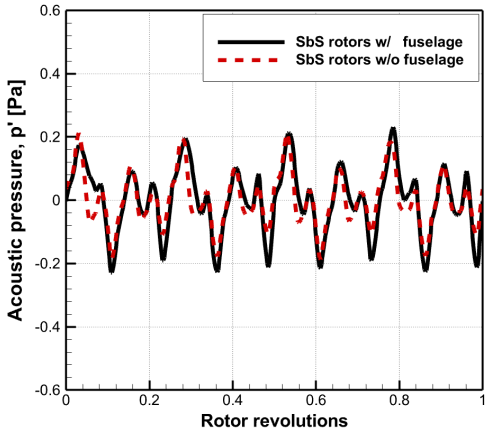

(c) Observer at Ψ_{MIC} = 180°

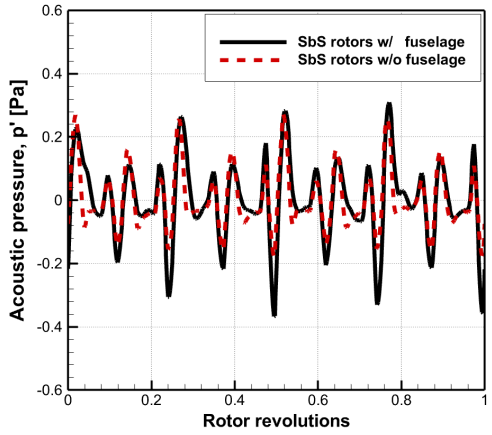

(d) Observer at Ψ_{MIC} = 270°

Fig. 12. Comparison of the overall acoustic pressure for isolated rotor and full configuration in hovering condition with OGE

Figure 13 shows the acoustic amplitude in decibels associated with the BPF at the fore, port, aft, and starboard sides of the aircraft for both the full configuration and isolated rotor cases under OGE conditions. The first BPF (i.e., the fundamental frequency) is defined as the rotational frequency of the rotor multiplied to the number of blades. The fundamental frequency of the four-bladed rotor on the starboard of the SbS rotor system is approximately 33 Hz. Fig. 13 demonstrates that tonal noise for both cases occurred at even harmonics, particularly within low-frequency ranges. This suggests that rotor-to-rotor blade-vortex interactions are the primary noise source in the overlapped side-by-side rotor system, as also reported in references [36, 37]. Moreover, this figure shows the presence of fuselage increases the sound pressure level of UAM aircraft. This increase is less evident

for the observer at azimuth angle of 180°, where the fuselage has less effect on the acoustic behavior of the rotor system. In the full configuration case for the observer at ψ_{MIC} = 0°, the peak SPL occurs at the sixth harmonic, whereas it occurs at the second harmonic for the isolated rotor system. Moreover, owing to the increase in the interactions between the blade and vortices, in this direction, for higher frequencies (6^{th}–20^{th} BPFs), the SPL is also higher for the full configuration case. The peak SPL for microphone at ψ_{MIC} = 180°, occurs at the second harmonics. The observers at the lateral sides of the rotor system (Fig. 13 (b) and Fig. 13 (d)), the fuselage similarly influences the rotor system noise emissions in both directions, where the peak SPL occurs at the fourth harmonic.

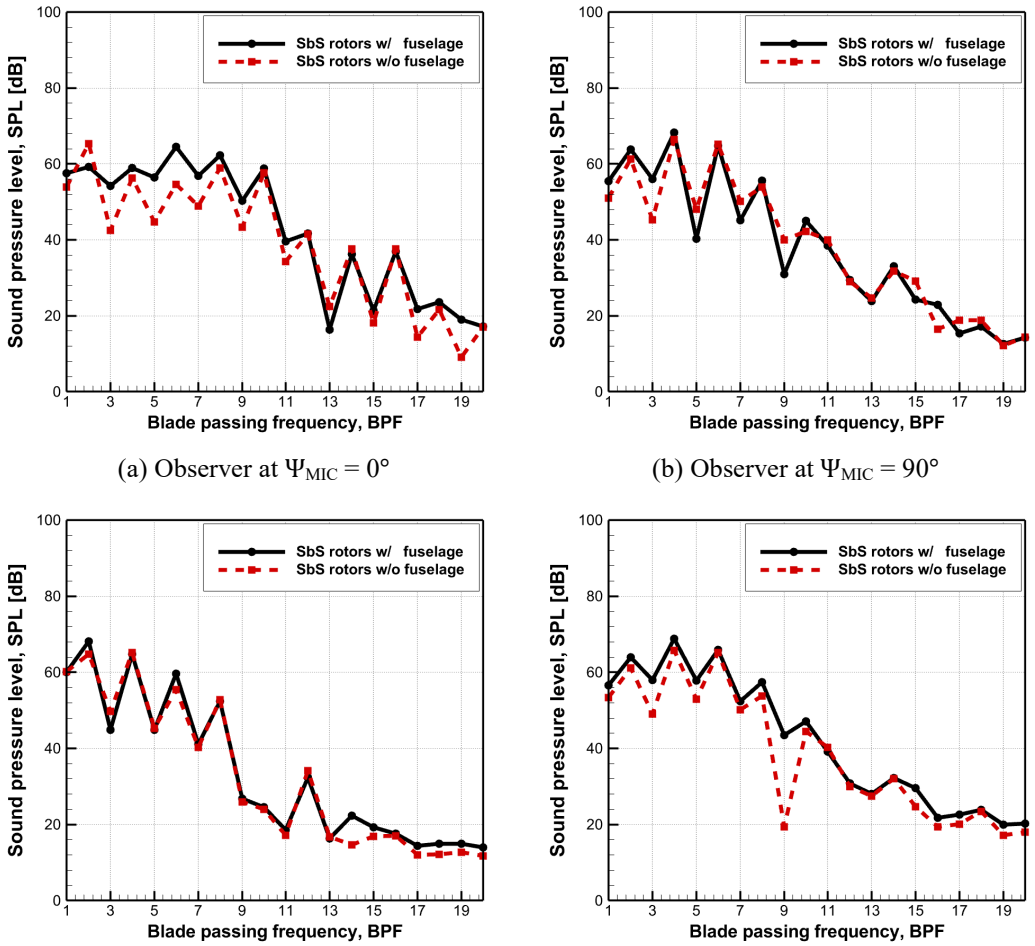

(a) Observer at Ψ_{MIC} = 0°

(b) Observer at Ψ_{MIC} = 90°

(c) Observer at Ψ_{MIC} = 180°

(d) Observer at Ψ_{MIC} = 270°

Fig. 13. Comparison of sound pressure level associated with blade passing frequency for isolated rotor and full configuration in hovering condition with OGE

Figure 14 compares the overall sound pressure levels (OASPL) directivity of the full configuration and isolated rotor to analyze the acoustic radiation characteristics with and without the fuselage. In the full configuration, the

maximum and minimum OASPL values are 64 dBA and 57 dBA, respectively. By contrast, these values are only approximately 62 dBA and 56 dBA for the isolated rotor configuration, respectively. Consequently, the fuselage effect results in an average increase of 2 dBA in the OASPL over all microphones compared with the isolated rotor. However, the noise level is influenced by the presence of the fuselage slightly more in the aftward direction of the rotorcraft, where vortices reflected from the airframe lead to stronger BVIs. In this area, the model predicts an almost 4 dB(A) increase in the OASPL for the rotorcraft with the fuselage. For both cases, the observer at ψ_{MIC} = 180° experiences the minimum OASPL, where it can be seen the fuselage has less effect on the rotorcraft OGE (about 1 dBA).

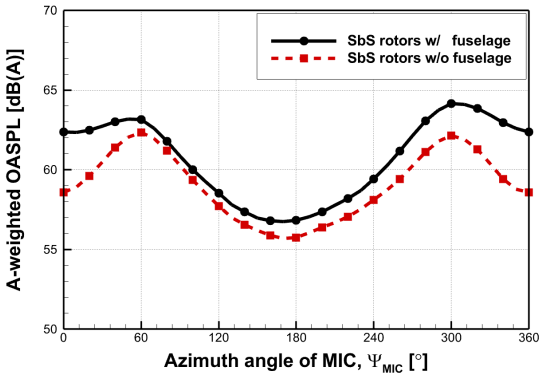

Fig. 14. Comparison of A-weighted overall sound pressure levels (OASPL) for isolated rotor and full configuration aircraft at various observer positions

4.2 Ground effect on the aerodynamics of SbS eVTOL

This section examines the aerodynamic performance of the SbS aircraft during hovering above the ground. Cases 3 and 4 (defined in Table 5) are selected in which the rotorcraft hovers above the ground with a fixed RPM at different heights from the ground (h/R = 1 and h/R = 2, respectively). Figure 15 shows the aerodynamic load of the rotor blades for a full-configuration aircraft hovering above the ground in one revolution, depending on the height from the ground. As expected, the closer the aircraft is to the ground, the higher the average thrust generated. Moreover, the amplitude of vibration slightly changes for h/R = 1 compared with that for h/R = 2. Moreover, the tip vortices in the overlapped region merged for the overlapped rotor, creating stronger vortices and leading to a higher downwash between the two rotors. The influence of this wake distortion is manifested by the azimuthal distribution of the thrust force on the rotor plane, as shown in Fig. 16. It can be observed that the rapid variation in the loading distribution in the overlapping region between the rotors with significant impulsive changes in the loading at the entrance (ψ = 150°) and exit (ψ = 212°) of the overlapped area for both rotors. This could stem

from the interaction of the tip vortices of one rotor experiencing near parallel interaction with the blade of the other rotor. When the rotorcraft is closer to the ground, higher upwash at the at aft side of the rotorcraft increases the loading distribution at the rear part of the rotor.

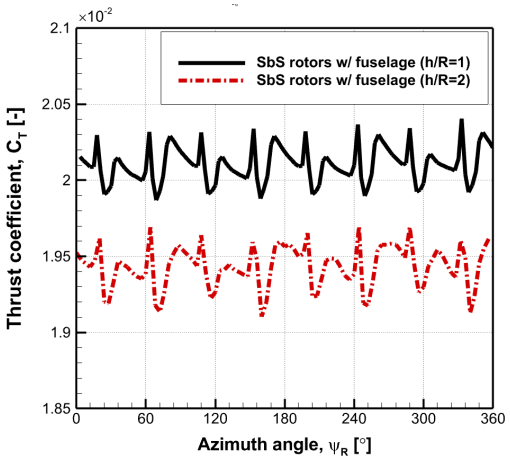

Fig. 15. Time variation in thrust coefficient for one rotor revolution of full configuration in IGE conditions

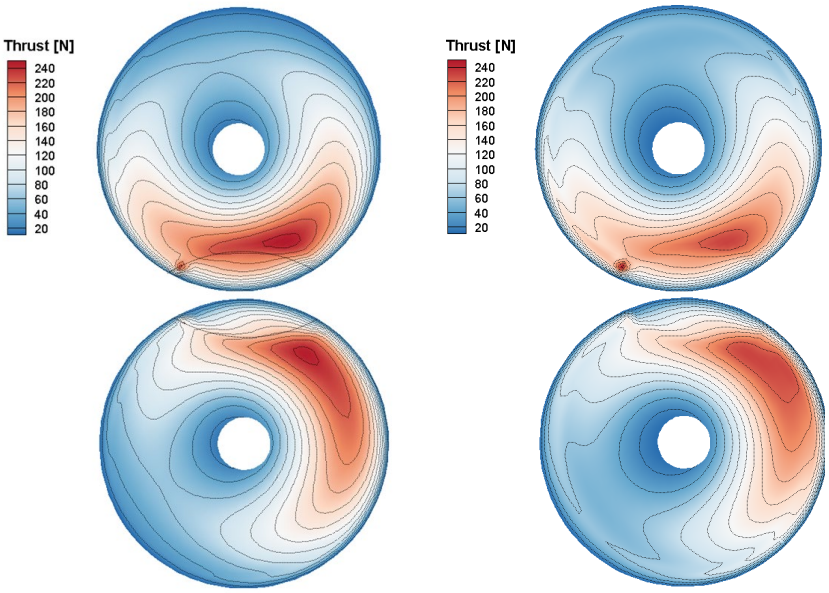

(a) Full configuration at h/R=1 (b) Full configuration at h/R=2

Fig. 16. Distribution of sectional thrust contour on the starboard (upper) and port (lower) rotor blades of full configuration in IGE conditions

Figure 17 compares the instantaneous velocity magnitudes for the hovering mode at two distances from the ground in the midplane, showing the development of strong vortices behind the rotorcraft. A vortex flow forms below the rotor system for h/R = 2. As the rotorcraft approaches the ground, the center of recirculation is pushed

farther from the centroid of the rotors. Ramasamy et al. [27] showed that the fuselage design could also affect the location of recirculation near the ground by performing experiments on tandem rotors. Comparing the velocities in the two cases indicates that the outwash is higher when the rotorcraft is closer to the ground. Comparing the velocity fields for h/R = 1 and h/R = 2 with the rotorcraft OGE in Fig. 8(a) reveals that the recirculation vortex gains more strength as the aircraft approaches the ground. A side view of the wake field for all ground effect cases is illustrated in Fig. 18. Strong recirculation occurs downward due to the rotating direction effect of the rotors. At h/R = 1, the recirculation above the rotor system increases the wake interactions. Moreover as the rotorcraft gets closer to the ground the decrease in the downwash velocity and the upwash flow due to the presence of the fuselage results in an increase in thrust of UAM aircraft. As the rotorcraft moves farther from the ground, the recirculation remains below the rotor plane, and the impact of the ground on the rotor performance diminishes (see Fig. 18(b)). Fig. 19 shows the induced inflow ratio at z/R = 0.12 in lateral direction. This figure indicates shows as the rotorcraft gets closer to the ground the downwash flow decreases more, which accordingly results in the increase in the thrust of the UAM aircraft.

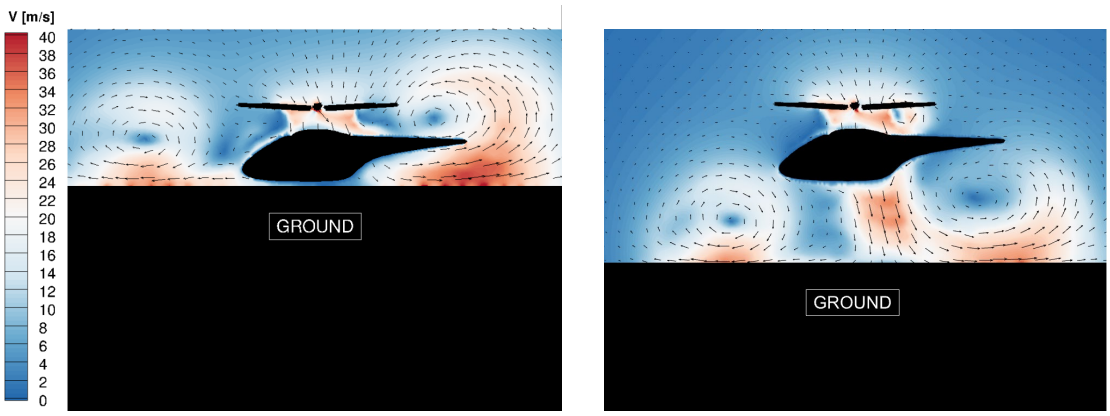

(a) Full configuration, h/R=1 (b) Full configuration, h/R=2

Fig. 17. Comparison of the instantaneous velocity magnitude contour of full configuration in IGE conditions

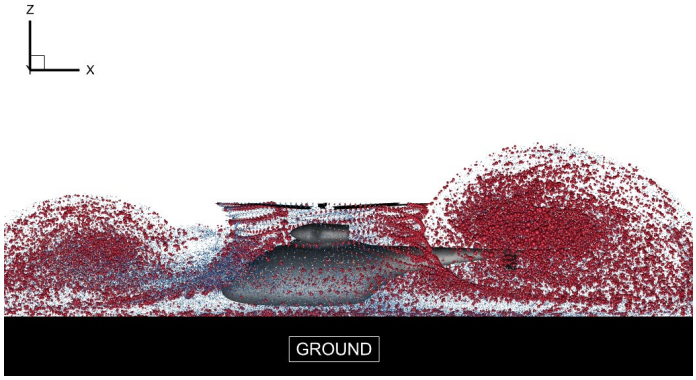

(a) Full configuration, h/R=1

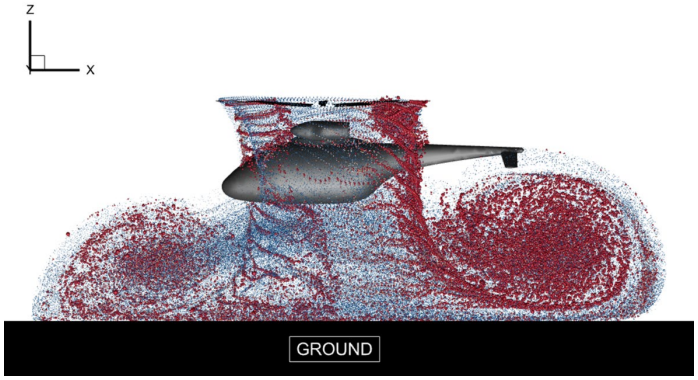

(b) Full configuration, h/R=2

Fig. 18. Comparison of wake structures of full configuration in IGE conditions

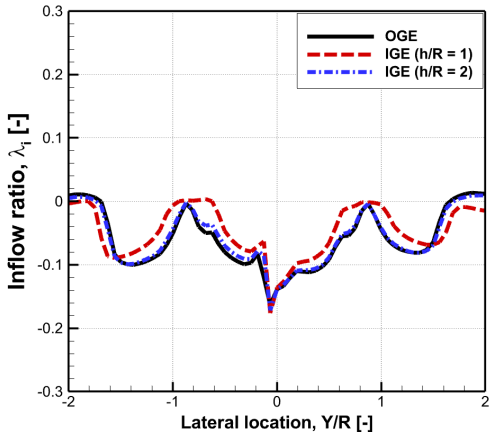

Fig. 19. Comparison of induced inflow ratio of full configuraiton in IGE conditions at z/R = 0.12 along the lateral direction

4.3 Ground effect on the acoustics of SbS eVTOL

This section discusses the effects of the ground on the noise characteristics of the SbS eVTOL aircraft at different heights from the ground (h/R = 1 and h/R = 2). The microphone array with a circular arrangement of 36 microphones and a radial distance of 50 m (≈8R) was placed in the rotor disk plane to explore the variations in the noise characteristics with varying ground proximity (see Fig. 7(b)). The SPLs radiating from the SbS rotor system at the observer locations on the aft (ψ_{MIC} = 0°), starboard (ψ_{MIC} = 90°), fore (ψ_{MIC} = 180°), and port (ψ_{MIC} = 270°) sides of the UAM aircraft are depicted in Fig. 20. The total acoustic pressures of the full configuration at different heights from the ground are compared with the aircraft results under OGE conditions. The total acoustic pressure on the rotating plane is the sum of the thickness and loading noise components. As discussed in relation to Fig. 16(a), an increase in the overall SPL and many impulsive changes in the sound pressure occur due to the BVI for the microphone located at ψ_{MIC} = 0° as the rotorcraft approaches the ground. Fig. 20 illustrates that although the existence of ground has an insignificant effect on the low-frequency acoustic pressure signals. However, the ground intensifies the high-frequency noises propagated from the blade, especially in the fore side direction of the aircraft. The acoustic pressure on the fore side (ψ_{MIC} = 180°) of the SbS aircraft is the lowest among that on the other sides because the rotor wake propagates to the back of the aircraft, and the most pronounced interactions occur on the aft side (ψ_{MIC} = 0°). The magnitude of the acoustic pressure for the observer at ψ_{MIC} = 270° is slightly different from that for the observer at ψ_{MIC} = 90°, with higher absolute values of the peaks on the port side of the rotor system.

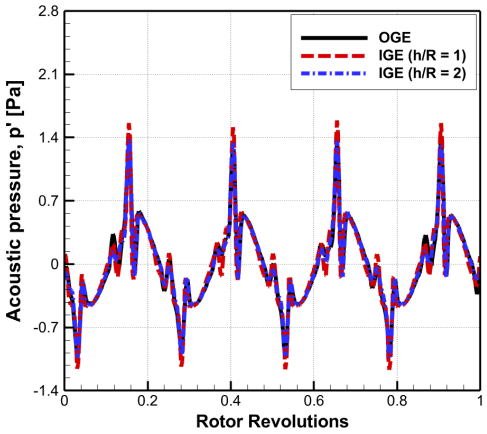

(a) Observer at Ψ_{MIC} = 0°

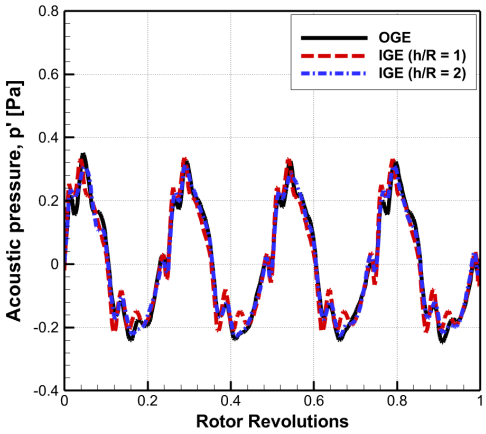

(b) Observer at Ψ_{MIC} = 90°

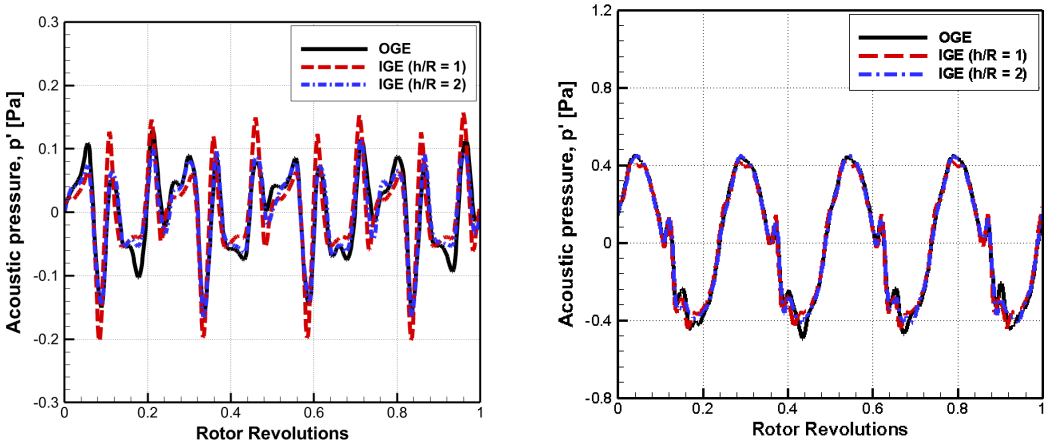

(c) Observer at Ψ_{MIC} = 180°

(d) Observer at Ψ_{MIC} = 270°

Fig. 20. Comparison of the overall acoustic pressure for hovering UAM aircraft in ground effect (IGE) at h/R=1 and h/R=2

The results for the first 20 blade-passing frequencies are shown in Fig. 21. The highest noise level in the spectrum for the observers at all the positions except the observer at ψ_{MIC} = 180° occurs at the first BPF. The dominant noise signal on the aft side of the aircraft is approximately 82 dB, which is almost 18 dB higher than the SPL recorded by the observer on the fore side of the aircraft. This difference slightly increases as the rotorcraft gets closer to the ground due to the stronger upwash wake, which results in more intense blade vortex interaction, particularly on the aft side of the rotorcraft. The figure shows that moving closer to the ground does not affect the low-frequency signals on the aft side of the SbS aircraft, at which its fuselage has a more dominant influence. For the microphone on the fore side, for which the fuselage influence is the lowest, the signal levels vary more noticeably as the altitude of the aircraft changes. Fig. 21 also demonstrates that, as the frequencies of the noise signals increase (after the sixth harmonics), the influence of the ground on the noise intensity also increases. The figure shows for the observer at ψ_{MIC} = 0° and ψ_{MIC} = 180°, especially for low-frequency noises, the tonal noise occurred at the odd harmonics, suggesting that the interaction between a rotor and upwash flow is the dominant noise source. However, for the observer at the starboard and port sides of the rotorcraft, and as the rotorcraft gets closer to the ground (for high-frequency noises, especially for the microphone at ψ_{MIC} = 180°), the tonal noise increases at both odd and even harmonics, which suggests that the rotor-rotor interaction noise is also a dominant noise source in addition to the interaction between a rotor and upwash. These higher harmonic tonal noise components originate from the growth of vortex interactions as the aircraft approaches the ground, as manifested in the wake field of the rotorcraft near the ground (See Fig. 18).

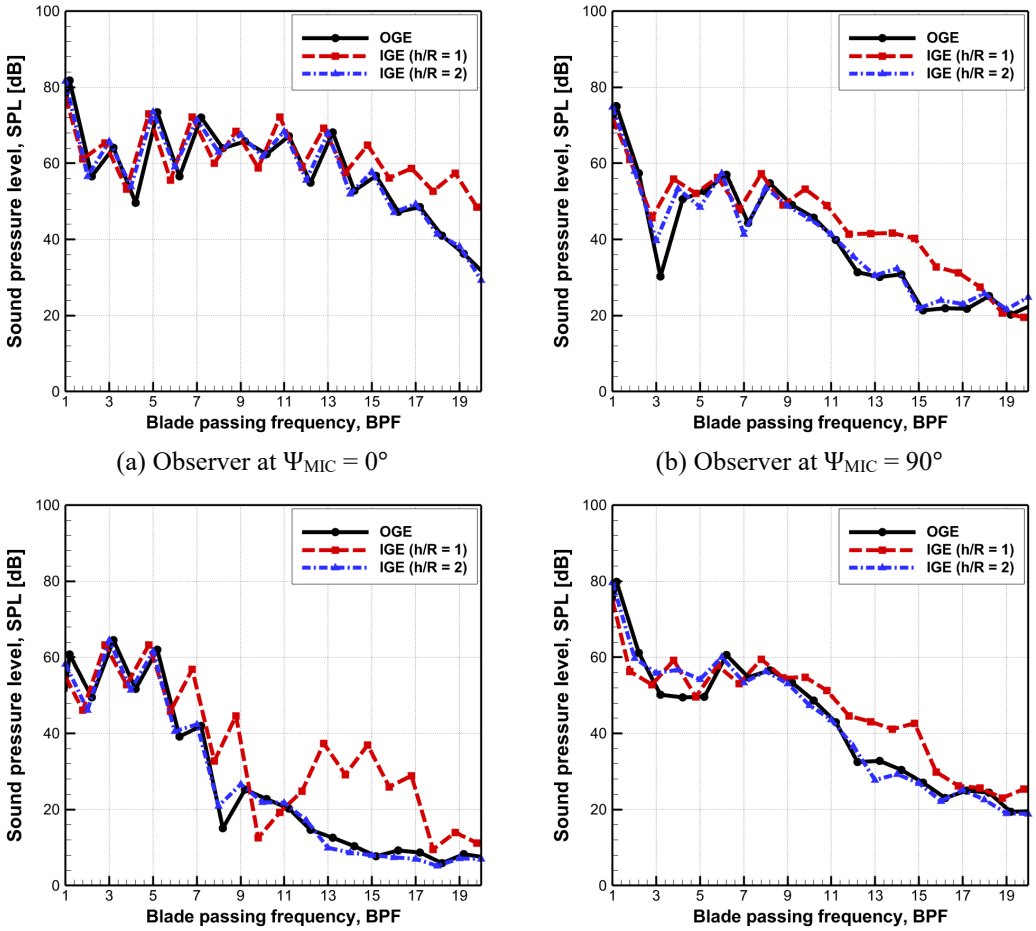

(a) Observer at Ψ_{MIC} = 0°

(b) Observer at Ψ_{MIC} = 90°

(c) Observer at Ψ_{MIC} = 180°

(d) Observer at Ψ_{MIC} = 270°

Fig. 21. Sound pressure level-blade passing frequency for hovering UAM aircraft for all the cases in ground effect (IGE) for the observers at the rotor plane

The interaction between the ground recirculation and recirculation vortex flow from the fuselage increases the weak, high-frequency tonal noises. However, this interaction may cause cancelation in certain directions, resulting in a lower SPL at certain noise frequencies. To demonstrate the effect of the ground on the high-frequency noise further, this noise was categorized into low (1^{th}–5^{th} BPFs) and high (6^{th}–20^{th} BPFs) frequency signals for which the resultant logarithmic sum of sound pressure levels at each microphone is calculated and presented in Fig. 22. This figure indicates that the resultant low-frequency noise for the observer at $\psi_{mic} = 0°$ is almost 3 dB higher than the noise recorded for the port and starboard side microphones and approximately 15 dB higher than the resultant noise for the fore side microphone. However, the difference between the resultant high-frequency sound pressure level recorded at the microphone at $\Psi_{Mic} = 0°$ and other microphones are more than 14 dB, which indicates the high blade vortex interactions and intense unsteadiness of the wake field in the aft direction of the rotorcraft. Furthermore, the ground has insignificant effects on the low-frequency tonal components. In contrast,

for the high-frequency tones, the ground leads to an elevation of sound pressure level, about 13 dB for the microphone at ψ_{MIC} = 180° and 2 dB for the other three microphones, where the influence of the fuselage is more pronounced.

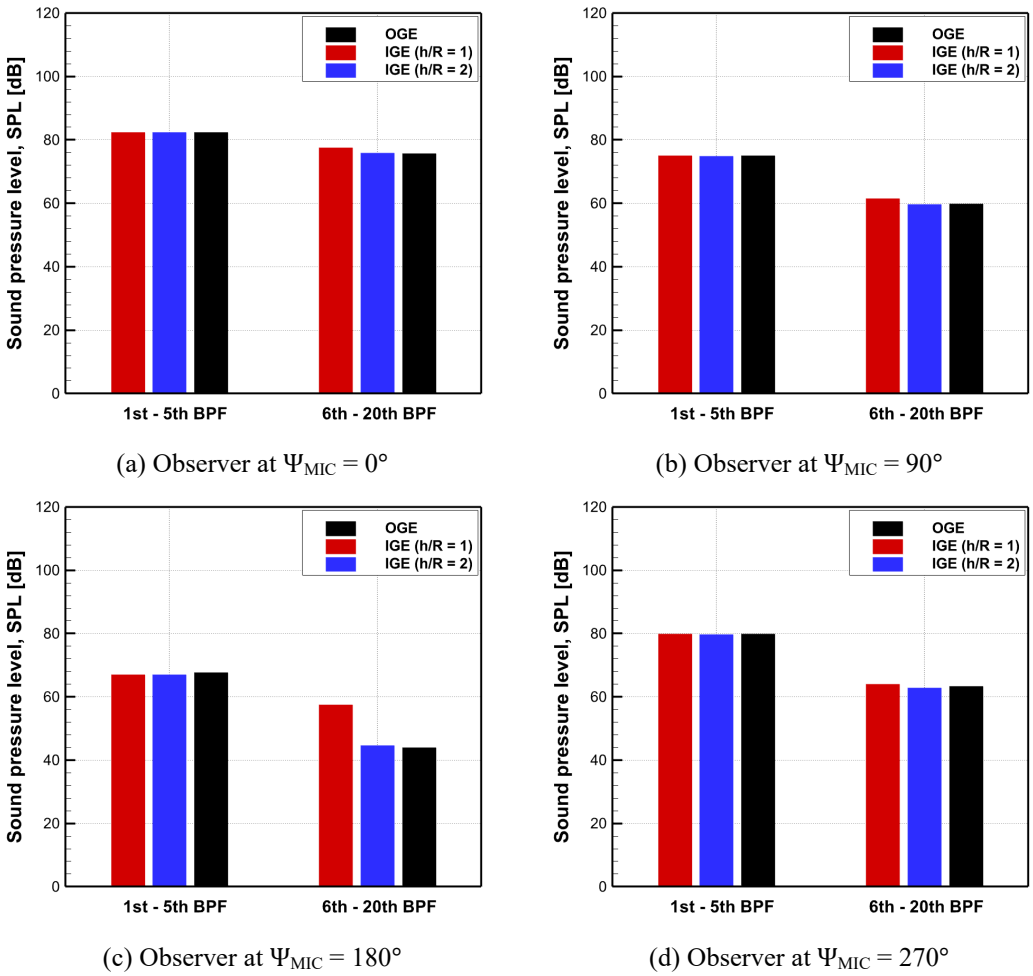

(a) Observer at Ψ_{MIC} = 0°

(b) Observer at Ψ_{MIC} = 90°

(c) Observer at Ψ_{MIC} = 180°

(d) Observer at Ψ_{MIC} = 270°

Fig. 22. Accumulated sound pressure levels calculated from 1st-5th BPF and 6th-20th BPF

Figure 23 compares OASPL directivity of a hovering SbS aircraft under IGE and OGE conditions. The OASPL is calculated for the observers at a radial distance of 50 m (≈8*R*) away from the center of the rotor system in the rotor plane, as defined in Fig. 7. Under both IGE and OGE conditions, the difference between the maximum and minimum OASPLs is approximately 24 dBA, which indicates a significant difference in the noise level based on the location of the observer relative to the aircraft. For the rotorcraft closer to the ground, the OASPL is 2–3 dBA higher for most observers around the aircraft. The directivity pattern of the OASPL does not change as the altitude of the aircraft decreases. However, the comparison results between the IGE with *h/R* = 2 and the OGE conditions show that a threshold height exists at which the impact of the ground on the aircraft is negligible. It can be inferred

that the noise levels are the highest for the microphones located downward relative to the SbS aircraft and gradually decrease as the observer approaches the nose of the aircraft.

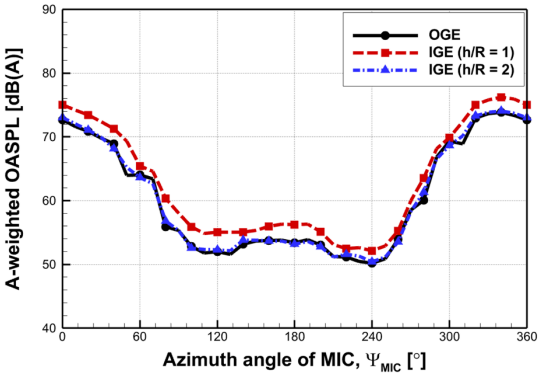

Fig. 23. A-weighted overall sound pressure levels (OASPL) of UAM aircraft in ground effect (IGE) at various observer positions

Figure 24 presents the three-dimensional (3D) directivity pattern of OASPL to provide a better understanding of the impact of the fuselage and the ground on the aeroacoustic characteristics of SbS UAM aircraft in hover flight. A noise hemisphere is positioned above the SbS UAM aircraft with a 50 m (≈8R) from the center of the vehicle, and it is discretized at 10° intervals for both azimuth and elevation angles. It can be observed that OASPL in the aft quadrant of the aircraft is higher than the forward quadrant. This is because of the higher loading that the rotors experience in their rear area due to the direction of rotation. Therefore, the maximum OASPL of the full configuration aircraft in both IGE and OGE conditions occurs behind the aircraft between 40 to 60 degrees above the rotor plane, while the minimum OASPL occurs in the forward of the aircraft between 0 to 30 degrees above the rotor plane. Moreover, the noise hemisphere illustrates a region of high OASPL above the rotor system resulting from the loading noise of the rotor blade. Comparing Figs. 24(a) and 24(b) show that the existence of fuselage leads to an increase in OASPL, especially above the rotor system, due to the stronger upwash wake by the airframe and the ground, as discussed in Fig. 10. Moreover, the noise directivity and maximum noise levels under OGE and IGE conditions with different height from the ground are compared to analyze the impact of ground effect on the noise of the SbS UAM aircraft in full configuration. It is evident that the OASPL increases in most directions as the SbS UAM aircraft approaches the ground, and the high OASPL region (denoted as red color) grows larger. A comparison of Fig. 24(b) and Fig 24(c), similar to the results shown in Fig. 23, when the distance from the ground was h/R = 2, the noise levels were comparable to those under OGE conditions, with similar the maximum OASPL values. However, the maximum OASPL increased by more than 3 dBA as the

altitude of the SbS UAM aircraft decreased to h/R = 1. The maximum OASPL on the noise hemisphere is 76.95 dBA at h/R = 2 conditions. As the aircraft moves closer to the ground under the h/R = 1 condition, the influence of the ground effect increases, resulting in a maximum OASPL of 80.45 dBA.

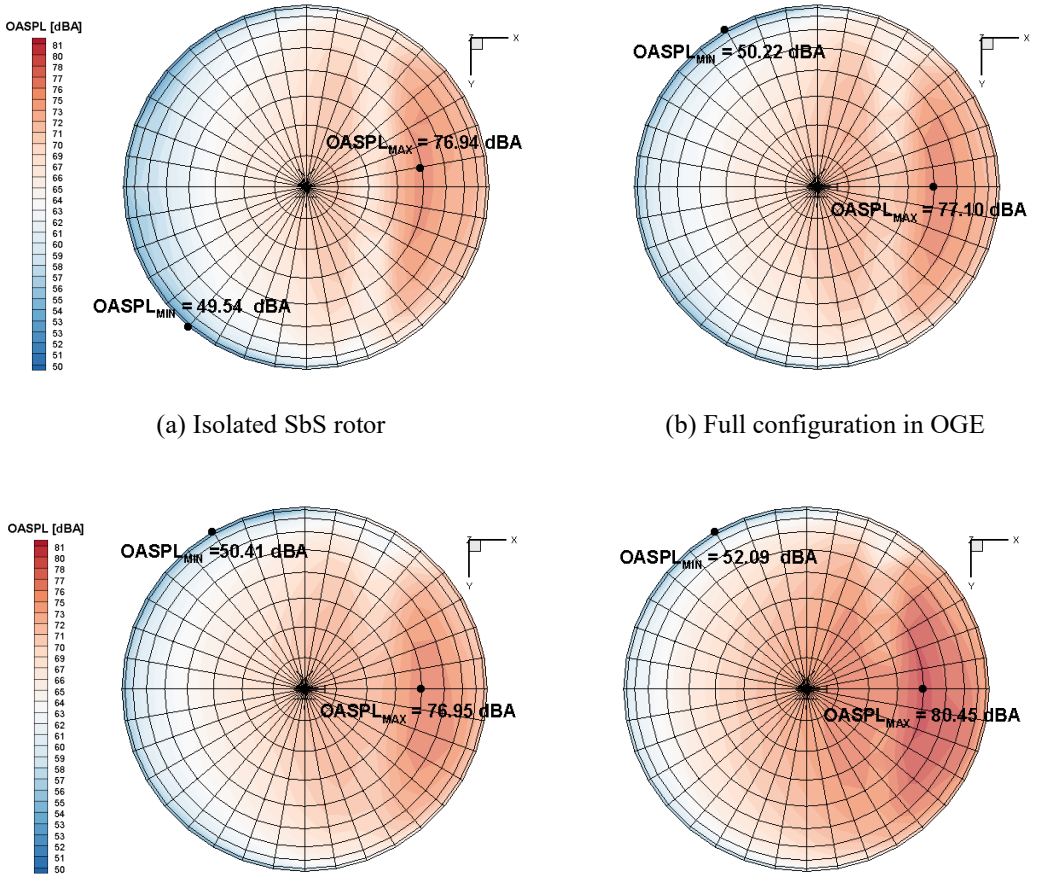

(a) Isolated SbS rotor

(b) Full configuration in OGE

(c) Full configuration in IGE, h/R=2

(d) Full configuration in IGE, h/R=1

Fig. 24. Three-dimensional representation of OASPL evaluated on the hemisphere above the rotor system with the radius of 50 m from the center of the rotors (bottom-side view).

5. Conclusion

This study investigates the effects of fuselage and ground on the aerodynamic and aeroacoustic performance of NASA's SbS UAM aircraft in full configuration using coupled vortex methods and FW-H acoustic analogy. The simulation results show that the existence of fuselage directly affects the wake field of the UAM vehicle and influences the aerodynamic loads acting on the rotor blades, acoustic signature, and noise directivity. These effects were observed under both IGE and OGE conditions. As the UAM aircraft approaches the ground, the SPL increases, and the impact of the fuselage becomes more noticeable due to the stronger upwash wake by the

airframe and the ground. It is found that the most pronounced effect of the ground on the noise characteristics of the aircraft is the high-frequency tonal noise, where the ground leads to an increase in the SPL, especially in the directions where the fuselage has less influence on the wake field. The high-frequency tone in the aircraft's aft direction is more intense than in other directions, indicating a stronger BVI related to the intense unsteadiness of the wake field in this direction of the rotorcraft. In the ground effect, the interaction between a rotor and upwash flow is the dominant source noise, especially for low-frequency noises for the observers at the fore and aft sides of the aircraft. However, for the observer at the starboard and port sides of the rotorcraft, the rotor-rotor interaction noise is also a dominant noise source in addition to the interaction between a rotor and the upwash flow. The noise hemisphere above the vehicle shows that as the altitude of aircraft gets closer to the ground, the OASPL increases for most of the directions, and the high OASPL region expands. Moreover, the OASPL in the aft quadrant of the aircraft is higher than the forward quadrant. This is because of the higher loading that the rotors experience in their rear area due to their direction of rotation. It was concluded that the ground effect causes the aerodynamic noise to increase by more than 3 dBA as the SbS UAM aircraft descends for landing and approaches the ground.

The results of the present method provide valuable insights into the flow physics, unsteady behavior of the wake field, and noise characteristics of the SbS UAM aircraft in full configuration hovering above the ground. Our findings demonstrate the importance of the fuselage design and rotor system configuration in the aeroacoustic performance of a UAM vehicle during its operation under both IGE and OGE conditions. This information can be used to develop advanced designs and operational guidelines for UAM vehicles to enhance their safety and acoustic comfort. Although the numerical model used in this study is an efficient way to simulate the full configuration of the UAM vehicle, it cannot accurately capture the non-deterministic acoustic components. In the future, we aim to couple vortex methods with the high-fidelity CFD based on the finite volume method to improve the predictive capability of vortex models while maintaining computational efficiency and predict the complicated flow around the rotorcraft and the flow-induced noise level.

Declaration of competing for interest

The authors declare that they have no known competing financial interests or personal relationships that could have appeared to influence the work reported in this paper.

Acknowledgments

This study was supported by the National Research Foundation of Korea (NRF) grant funded by the Ministry of Science and ICT (NRF-2021R1C1C1010198 and RS-2024-00397400). This research was supported by the regional innovation megaproject program through the Korea Innovation Foundation, funded by the Ministry of Science and ICT (Project Number: 2023-DD-UP-0026).

References

[1] Ang, L. Y. L., and Cui, F., "Remote Work: Aircraft Noise Implications, Prediction, and Management in the Built Environment," *Applied Acoustics*, Vol. 198, p. 108978, 2022. https://doi.org/10.1016/j.apacoust.2022.108978

[2] Can, A., L'Hostis, A., Aumond, P., Botteldooren, D., Coelho, M.C. Guarnaccia, C., Kang, J., "The future of urban sound environments: Impacting mobility trends and insights for noise assessment and mitigation," *Applied Acoustics*, Vol. 170, p. 107518, 2020. https://doi.org/10.1016/j.apacoust.2020.107518

[3] Rizzi, S. A., Huff, D. L., Boyd, Jr. D. D., Bent, P., Henderson, B. S., Pascioni, K. A., Sargent, D. C., Josephson, D. D., Marsan, M., He, H., "Urban Air Mobility Noise: Current Practice, Gaps, and Recommendations," NASA/TP–2020-5007433, 2020.

[4] Kim, J. H., "Urban Air Mobility Noise: Further Considerations on Indoor Space," *International Journal of Environmental Research and Public Health*, Vol. 19, No. 18, 2022. http://doi.org/10.3390/ijerph191811298

[5] Gojon, R., Jardin, T., and Parisot-Dupuis, H., "Experimental Investigation of Low Reynolds Number Rotor Noise," *The Journal of the Acoustical Society of America*, Vol. 149, No. 6, 2021, pp. 3813–3829. https://doi.org/10.1121/10.0005068

[6] Eißfeldt, H., "Sustainable Urban Air Mobility Supported with Participatory Noise Sensing," *Sustainability*, Vol. 12, No. 8, 2020. http://doi.org/10.3390/su12083320

[7] Lia, Y., Ma, Z., Zhoua, P., Zhang, S., Zhang, X., "A numerica linvestigation of the aerodynamic and aeroacoustic interactions between components of a multi-rotor vehicle for urban air mobility," *Journal of Sound and Vibration*, Vol. 571, p. 118002, 2024. https://doi.org/10.1016/j.jsv.2023.118002

[8] Zhanga, T., Barakos, G. N., Filipponec, A., Furqand, "High-fidelity aero-acoustic evaluations of a heavy-lift eVTOL in hover," *Journal of Sound and Vibration*, Vol. 584, p.118453, 2024. https://doi.org/10.1016/j.jsv.2024.118453

[9] Jia, Z., and Lee, S., "Computational Study on Noise of Urban Air Mobility Quadrotor Aircraft," *Journal of the American Helicopter Society*, Vol. 67, No. 1, pp. 1-15, 2022. https://doi.org/10.4050/JAHS.67.012009

[10] Jia, Z., and Lee, S., "Impulsive Loading Noise of a Lift-Offset Coaxial Rotor in High-Speed Forward Flight," *AIAA Journal*, Vol. 58, No. 2, pp. 687-701, 2020. https://doi.org/10.2514/1.J058295

[11] Pulliam, T., "High Order Accurate Finite-Difference Methods: As Seen in OVERFLOW," *Proceedings of the 20th AIAA Computational Fluid Dynamics Conference*, Honolulu, HI, 2011. http://doi.org/10.2514/6.2011-3851

[12] Brès, G. A., Brentner, K. S., Perez, G., and Jones, H. E., "Maneuvering Rotorcraft Noise Prediction," *Journal of Sound and Vibration*, Vol. 275, No. 3, 2004, pp. 719–738. https://doi.org/10.1016/j.jsv.2003.07.005

[13] Brentner, K. S., and Farassat, F., "Modeling Aerodynamically Generated Sound of Helicopter Rotors," *Progress in Aerospace Sciences*, Vol. 39, No. 2, pp. 83–120, 2003. http://doi.org/10.1016/S0376-0421(02)00068-4

[14] Ffowcs Williams, J. E., Hawkings, D. L., and Lighthill, M. J., "Sound Generation by Turbulence and Surfaces in Arbitrary Motion," *Philosophical Transactions of the Royal Society of London. Series A, Mathematical and Physical Sciences*, Vol. 264, No. 1151, pp. 321–342, 1997. http://doi.org/10.1098/rsta.1969.0031

[15] Ventura Diaz, P., and Yoon, S., "Computational Study of NASA's Quadrotor Urban Air Taxi Concept," *Proceedings of the AIAA SciTech 2020 Forum*, Orlando, FL, 2020. http://doi.org/10.2514/6.2020-0302

[16] Dbouk, T., and Drikakis, D., "Quadcopter Drones Swarm Aeroacoustics," *Physics of Fluids*, Vol. 33, No. 5, p. 57112, 2021.
http://doi.org/10.1063/5.0052505

[17] Jasak, H., "OpenFOAM: Open Source CFD in Research and Industry," *International Journal of Naval Architecture and Ocean Engineering*, Vol. 1, No. 2, pp. 89–94, 2009.
http://doi.org/10.2478/IJNAOE-2013-0011

[18] Ko, J., and Lee, S., "Quantification of Wake Interaction Effects on Multi-rotor Configurations in Forward Flight," *Aerospace Science and Technology*, Vol. 135, p. 108188, 2023.
http://doi.org/10.1016/j.ast.2023.108188

[19] Jeong, J., Ko, J., Cho, H., and Lee, S., "Random Process-Based Stochastic Analysis of Multirotor Hovering Noise Under Rotational Speed Fluctuations," *Physics of Fluids*, Vol. 33, No. 12, p. 127107, 2021.
http://doi.org/10.1063/5.0071850

[20] Gwak, D. Y., Han, D., and Lee, S., "Sound Quality Factors Influencing Annoyance From Hovering UAV," *Journal of Sound and Vibration*, Vol. 489, p. 115651, 2020.
http://doi.org/10.1016/j.jsv.2020.115651

[21] Ahuja, V., Little, D. S., Majdalani, J., and Hartfield, R. J., "On the Prediction of Noise Generated by Urban Air Mobility (UAM) Vehicles. II. Implementation of the Farassat F1A Formulation Into a Modern Surface-Vorticity Panel Solver," *Physics of Fluids*, Vol. 34, No. 11, p. 116118, 2022.
http://doi.org/10.1063/5.0105002

[22] Little, D. S., Majdalani, J., Hartfield, R. J., and Ahuja, V., "On the Prediction of Noise Generated by Urban Air Mobility (UAM) Vehicles. I. Integration of Fundamental Acoustic Metrics," *Physics of Fluids*, Vol. 34, No. 11, p. 116117, 2022.
https://doi.org/10.1063/5.0124134

[23] Kim, S. J., Hwang, Y.-H., Myong, R. S., and Lee, H., "Interactional Aerodynamics and Acoustics of a Rotor with an Airframe in Hover," *Physics of Fluids*, Vol. 36, No. 1, 2024, p. 17121.
https://doi.org/10.1063/5.0185036

[24] Lascara, B., Spencer, T., DeGarmo, M., and Lacher, A., "Urban Air Mobility Landscape Report Initial Examination of a New Air Transportation System," MITRE Corporation, 2018.

[25] Mayor, T., and Anderson, J., "Getting Mobility off the Ground," *KPMG*, 2020.

[26] Rovere, F., Barakos, G., and Steijl, R., "Safety Analysis of Rotors in Ground Effect," *Aerospace Science and Technology*, Vol. 129, p. 107655, 2022. http://doi.org/10.1016/j.ast.2022.107655

[27] Ramasamy, M., Potsdam, M., and Yamauchi, G. K., "Measurements to Understand the Flow Mechanisms Contributing to Tandem-Rotor Outwash," *Proceedings of the Annual Forum and Technology Display*, Virginia Beach, VA, 2018.

[28] Yunus, F., Casalino, D., Avallone, F., and Ragni, D., "Efficient Prediction of Urban Air Mobility Noise in a Vertiport Environment," *Aerospace Science and Technology*, Vol. 139, p. 108410, 2023. http://doi.org/10.1016/j.ast.2023.108410

[29] Andronikos, T., Papadakis, G., Riziotis, V., Prospathopoulos, J., and Voutsinas, S. G., "Validation of a Cost Effective Method for the Rotor-Obstacle Interaction," *Aerospace Science and Technology*, p. 106698, 2021. https://doi.org/10.1016/j.ast.2021.106698

[30] Silva, P. A. S. F., Tsoutsanis, P., and Antoniadis, A. F., "Numerical Investigation of Full Helicopter With and Without the Ground Effect," *Aerospace Science and Technology*, Vol. 122, p. 107401, 2022. http://doi.org/10.1016/j.ast.2022.107401

[31] Tan, J. F., Yon, T., He, L., Yu, L. J., and Wang, C., "Accelerated Method of Helicopter Brownout With Particle-Particle Collisions," *Aerospace Science and Technology*, Vol. 124, p. 107511, 2022. http://doi.org/10.1016/j.ast.2022.107511

[32] Garofano-Soldado, A., Sanchez-Cuevas, P. J., Heredia, G., and Ollero, A., "Numerical-Experimental Evaluation and Modelling of Aerodynamic Ground Effect for Small-Scale Tilted Propellers at Low Reynolds Numbers," *Aerospace Science and Technology*, Vol. 126, p. 107625, 2022. http://doi.org/10.1016/j.ast.2022.107625

[33] Ramasamy, M., "Hover Performance Measurements Toward Understanding Aerodynamic Interference in Coaxial, Tandem, and Tilt Rotors," *Journal of the American Helicopter Society*, Vol. 60, No. 3, pp. 1–17, 2015. http://doi.org/10.4050/JAHS.60.032005

[34] Tan, J. F., Ge, Y. Y., Zhang, W. G., Cui, Z., and Wang, H. W., "Numerical Study on Helicopter Brownout With Crosswind," *Aerospace Science and Technology*, Vol. 131, p. 107965, 2022. http://doi.org/10.1016/j.ast.2022.107965

[35] Silva, C., Johnson, W., and Solis, E., "Multidisciplinary Conceptual Design for Reduced-Emission Rotorcraft," in *AHS Specialists on Aeromechanics Design for Transformative Vertical Flight*, San Francisco, CA, 2018.

[36] Sagaga, J., and Lee, S., "Acoustic Predictions for Side-by-Side Air Taxi in Full Configuration," in AIAA AVIATION 2023 Forum, San Diego, CA, 2023. http://doi.org/10.2514/6.2023-4522

[37] Sagaga, J., and Lee, S., "High-fidelity computational study of aerodynamic noise of side-by-side rotor in full configuration," *Journal of Sound and Vibration*, Vol. 592, p. 118607, 2024. http://doi.org/10.1016/j.jsv.2024.118607

[38] Ventura Diaz, P., Johnson, W., Ahmad, J., and Yoon, S., "The Side-by-Side Urban Air Taxi Concept," *Proceedings of the AIAA Aviation 2019 Forum*, Dallas, TX, 2019, p. 2828. http://doi.org/10.2514/6.2019-2828

[39] Jia, Z., and Lee, S., "High-Fidelity Computational Analysis on the Noise of a Side-by-Side Hybrid VTOL Aircraft," *Journal of the American Helicopter Society*, Vol. 67, No. 2, pp. 022005, 2022. https://doi.org/10.4050/JAHS.67.022005

[40] Sagaga, J., and Lee, S., "Acoustic Predictions for Side-by-Side Rotor with Ground Effect," *Proceedings of the Vertical Flight Society 79th Annual Forum & Technology Display*, West Palm Beach, Florida, May 16–18, 2023. https://doi.org/10.4050/F-0079-2023-17947

[41] Lee, H., and Lee, D.-J., "Rotor Interactional Effects on Aerodynamic and Noise Characteristics of a Small Multirotor Unmanned Aerial Vehicle," *Physics of Fluids*, Vol. 32, No. 4, p. 47107, 2020. http://doi.org/10.1063/5.0003992

[42] Silva, C., and Johnson, W., "Practical Conceptual Design of Quieter Urban VTOL Aircraft," *Proceedings of the Vertical Flight Society 77th Annual Forum*, Virtual event, 2021, pp. 11–13.

[43] Lee, H., Sengupta, B., Araghizadeh, M. S., and Myong, R. S., "Review of Vortex Methods for Rotor Aerodynamics and Wake Dynamics," *Advances in Aerodynamics*, Vol. 4, No. 20, 2022. http://doi.org/10.1186/s42774-022-00111-3

[44] Katz, J., and Plotkin, A., *Low-Speed Aerodynamics*, Cambridge University Press, Cambridge, UK, 2001.

[45] Winckelmans, G. S., and Leonard, A., "Contributions to Vortex Particle Methods for the Computation of Three-Dimensional Incompressible Unsteady Flows," *Journal of Computational Physics*, Vol. 109, No. 2, pp. 247–273, 1993. http://doi.org/10.1006/jcph.1993.1216

[46] Brentner, K. S., "Prediction of Helicopter Rotor Discrete Frequency Noise for Three Scale Models," *Journal of Aircraft*, vol. 25, no. 5, pp. 420–427, 1988. http://doi: 10.2514/3.45598

[47] Lee, H., and Lee, D.-J., "Noise Prediction of Multi-Rotor Unmanned Aerial Vehicle Considering Wake Interaction Effects," *Proceedings of the Vertical Flight Society's 75th Annual Forum & Technology Display*, Philadelphia, PA, 2019.

[48] Lee, H., and Lee, D.-J., "Effects of Platform Motions on Aerodynamic Performance and Unsteady Wake Evolution of a Floating Offshore Wind Turbine," *Renewable Energy*, Vol. 143, pp. 9–23, 2019. http://doi.org/10.1016/j.renene.2019.04.134

[49] Lee, H., and Lee, D.-J., "Numerical Prediction of Aerodynamic Noise Radiated From Quadcopter Unmanned Aerial Vehicles," *Proceedings of the Noise Control Engineering National Conference*, San Diego, CA, 2019, pp. 2286–2291.

[50] Chaffin, M. S., and Berry, J. D., "Navier-Stokes and Potential Theory Solutions for a Helicopter Fuselage and Comparison With Experiment," ATCOM Technical Report 94-A-013, 1994.

[51] O'Brien Jr, D. M., "Analysis of Computational Modeling Techniques for Complete Rotorcraft Configurations," Doctoral Dissertation, Daniel Guggenheim School of Aerospace Engineering, 2006.

[52] Light, J. S., "Tip Vortex Geometry of a Hovering Helicopter Rotor in Ground Effect," *Journal of the American Helicopter Society*, Vol. 38, No. 2, pp. 34–42, 1993. http://doi.org/10.4050/JAHS.38.34

[53] Phillips, C., Kim, H. W., and Brown, R. E., "The Flow Physics of Helicopter Brownout," *Proceedings of the 66th American Helicopter Society Forum: Rising to New Heights in Vertical Lift Technology*, Fairfax, VA, 2010.

[54] Filippone, A., *et al.*, "Rotor Wake Modelling in Ground Effect Conditions," *Proceedings of the 37th European Rotorcraft Forum*, Vergiate and Gallarate, Italy, 2011.

[55] Sitaraman, J., *et al.*, "Helios User Guide V. 8.0," *Aviation Development Directorate*, 2016.

[56] Litherland, B., and Holland, S., "NASA Urban Air Mobility (UAM) Reference Vehicles," National Aeronautics and Space Administration.

[57] Sagaga., J., and Lee, S., "Performance, Aerodynamics, and Aeroacoustics of Side-by-Side Rotors Using High-Fidelity Computational Fluid Dynamics," AIAA Journal, vol. 61, no. 12, pp. 5429–5445, Sep. 2023, http://doi.org/10.2514/1.J062955

[58] Ventura Diaz, P., Johnson, W., Ahmad, J., and Yoon, S., "Computational Study of the Side-by-Side Urban Air Taxi Concept," *Proceedings of the Vertical Flight Society's Annual Forum and Technology Display*, Philadelphia, PA, USA, 2019.

[59] Silva, C., Johnson, W. R., Solis, E., Patterson, M. D., and Antcliff, K. R., "VTOL Urban Air Mobility Concept Vehicles for Technology Development," *Proceedings of the 2018 Aviation Technology, Integration, and Operations Conference*, 2018, p. 3847. http://doi.org/10.2514/6.2018-3847

[60] Healy, R., McCauley, J., Gandhi, F., and Sahni, O., "A Computational Examination of Side-by-Side Rotors in Ground Effect," *Journal of the American Helicopter Society*, Vol. 68, No. 3, pp. 32007–32024, 2023. http://doi.org/10.4050/JAHS.68.032007